


12-2018

Exfoliation, Synthesis, and Characterization of Nanoscale Te

Takayuki Hironaka

University of Arkansas, Fayetteville

Follow this and additional works at: <https://scholarworks.uark.edu/etd>

 Part of the [Electronic Devices and Semiconductor Manufacturing Commons](#), and the [Engineering Physics Commons](#)

Recommended Citation

Hironaka, Takayuki, "Exfoliation, Synthesis, and Characterization of Nanoscale Te" (2018). *Theses and Dissertations*. 3086.
<https://scholarworks.uark.edu/etd/3086>

This Thesis is brought to you for free and open access by ScholarWorks@UARK. It has been accepted for inclusion in Theses and Dissertations by an authorized administrator of ScholarWorks@UARK. For more information, please contact scholar@uark.edu, ccmiddle@uark.edu.

Exfoliation, Synthesis, and Characterization of Nanoscale Te

A thesis submitted in partial fulfillment
of the requirements for the degree of
Master of Science in Electrical Engineering

by

Takayuki Hironaka
Osaka University
Bachelor of Engineering in Applied Physics, 2010
Osaka University
Master of Engineering in Applied Physics, 2012

December 2018
University of Arkansas

This thesis is approved for recommendation to the Graduate Council.

Gregory J. Salamo, PhD
Thesis Director

Hugh O. H. Churchill, PhD
Thesis Director

Shui-Qing Yu, PhD
Thesis Director

Hameed A. Naseem, PhD
Committee Member

Samir M. El-Ghazaly, PhD
Committee Member

Abstract

Since the experimental discovery of graphene, two dimensional materials have enjoyed more attention and emphasis in academic research than nanowires, but the latter are an important area of study for creating 1D materials, or single atom chains, the next generation materials for advancing electronic devices. Atomically thin layers can be generated from 2D materials with weak bonds in one direction, and by applying this concept to one dimensional weakly bonded materials, we hypothesize that single atom chains with atomic-scale diameters may be produced. Tellurium (Te) and selenium (Se) have lattices consisting of spiral chains oriented along the c-axis, and each chain weakly bonds with others to form a bulk crystal. Since Te exhibits higher mobility than Se, nanoscale Te was the primary focus of this work.

Trigonal Te single crystals were exfoliated, without tape, on oxidized silicon substrates. Atomic force spectroscopy revealed that Te nanowires with heights of only 1–2 nm and widths less than 100 nm were successfully fabricated. Anisotropic Te flakes with a thickness of 15 nm showed ridges running along the length of the flake surfaces. A₁ and E Raman modes of a 30 nm thick flake were consistent with those of bulk Te, but they showed a slight blueshift (4 cm⁻¹). Polarized Raman spectroscopy was used to determine the crystal orientation of the flakes.

Te and Se crystals were also grown on SiO₂ substrates by physical vapor deposition. Te flakes and wires with heights of 60 nm and 30 nm were obtained; Se flakes with a height of 30–40 nm were also obtained. The synthesized Te wires were utilized in electron transport measurements. A four-terminal device showed a mobility of 51 cm²V⁻¹s⁻¹ at 2.8 K, a mobility lower than predicted due to the low quality of the Te wire. The contact resistance and resistivity of Te were estimated to be 9.4 kΩ and 9.4×10⁻⁴ Ω·m by applying a correction factor of 0.6. Another successfully fabricated two-terminal device showed a mobility of 1032 cm²V⁻¹s⁻¹ at 10

K, which is a promising enough result to suggest that such a device could be used for quantum transport measurements.

Acknowledgment

I would like to express my deep gratitude and sincere thanks to Dr. Hugh O. H. Churchill for his continuous support and advice throughout my Master's study and research. Furthermore, I would like to thank Dr. Shui-Qing Yu and Dr. Gregory J. Salamo for their support over the past two years and the rest of my thesis committee, Dr. Hameed A. Naseem and Dr. Samir M. El-Ghazaly, for helping to review and critique this research. I would also like to acknowledge and thank Dr. Ishiang Shih, who provided single crystal tellurium, Dr. Jin Hu, who helped me with using furnaces, Rabindra Basnet, Krishna Pandey, who performed physical vapor deposition of Te and Se onto substrates, Mohammad Zamani Alavijeh, who aided with my AFM measurements, and Xian Hu, who helped me with my Raman spectroscopy measurements. I am grateful also to Dr. Satish Shetty for our many discussions about research, to Arash Fereidouni for all of his help, especially with the optical cryostat, and to my other lab members Hasan Doha, Josh Thompson, Jeb Stacy, and Shiva Davari. Thank you Thach Ngoc Pham, Yiyin Zhou, Huong Tran, and Joshua Grant for helping me so much when I started working in Dr. Yu's lab group. Finally, I'd like to sincerely thank my friends and family for their love and support throughout my Master's degree.

My research and accomplishments over the past two years would not have been possible without each and every one of you, and I am so grateful to have spent this chapter of my life with you all.

Parts of chapter 2 were originally published as

(1) H. O. H. Churchill et al., "Toward Single Atom Chains with Exfoliated Tellurium,"

Nanoscale Research Letters, vol. 12, Aug 10 2017

Table of Contents

Chapter 1 Introduction	1
1.1 Nanoscale and ballistic transport	1
1.2 Motivation	4
1.2 Background about tellurium.....	6
1.3 Organization	7
Chapter 2 Mechanical exfoliation of single crystal tellurium	8
2.1 Introduction.....	8
2.2 Mechanical exfoliation.....	8
2.3 Te flake.....	9
2.4 Ultra-thin Te wire.....	10
2.5 Oxygen plasma effect on tellurium flakes.....	14
2.5.1 Height of Te flake	14
2.5.2 Raman intensity.....	17
2.6 The challenge of Te exfoliation.....	19
Chapter 3 Physical vapor deposition of tellurium and selenium	20
3.1 Introduction.....	20
3.2 Physical vapor deposition on SiO ₂ substrates	20
3.3 Characterization of deposited tellurium and selenium	21
3.3.1 Tellurium	21
3.3.2 Selenium	26
3.4 Annealing of r-plane sapphire substrates.....	29
3.5 Physical vapor deposition on atomic step substrates	32
Chapter 4 Transport measurement of Te wire	35
4.1 Introduction.....	35
4.2 Device fabrication	35
4.3 Measurement set-ups.....	39
4.4 I-V curve	41
4.5 Contact resistance and resistivity of device 2-SF.....	45
4.6 Conductance	49
4.7 Magnetic field dependence of device 2-SF conductance	52
4.8 Mobility	56

Chapter 5 Summary and future work	58
5.1 Summary.....	58
5.2 Future work.....	59
References	60
Appendix	67

Chapter 1 Introduction

1.1 Nanoscale and ballistic transport

Semiconductor nanowires have been extensively investigated for their unique electrical, optical, and mechanical properties. Compared to bulk crystal material, the nanoscale size of nanowires and the many properties related to their small scale make them an attractive material for application in a broad range of fields such as chemical sensors [1-3], lasers [4-6], photodetectors [7, 8], and transistors [9-11]. Simply scaling down a certain device from two dimensions to one dimension enables the fabrication of higher density devices while still following Moore's law. And from an electrical and physical property standpoint, electron transport in nanowires is classified as a mesoscopic system under certain conditions such as low temperature and low bias voltage. One important phenomenon is the ballistic transport with quantized conductance.

The first quantized conductance was observed in the two-dimensional electron gas (2DEG) of a GaAs-AlGaAs heterojunction by applying a point contact structure [12, 13]. In this regime, electrons were repelled by the negative gate voltage, and thus conductance decreased by taking the step values of $\frac{e^2}{h}$ with increasing negative gate voltage (Figure 1.1). The conductance quantum, $\frac{e^2}{h}$, was obtained by taking into account the one-dimensional (1D) density of states [12]. We assume that there is no scattering within the wire of length L , treating it as a single 1D subband. Generally, the density of states is defined as

$$g(E) = \frac{\partial N}{\partial E} = \frac{\partial N}{\partial k} \frac{\partial k}{\partial E} \quad (1.1)$$

where N is the total number of states, k is the wave number, and E is the energy. The total number of states N in an one-dimensional system is calculated by accounting for k -space [14].

The volume of a wire in k -space is either positive or negative k , depending on the current flow, and the volume occupied by one state is $\frac{2\pi}{L}$. Thus, the total number of states N is

$$N = g_s k \frac{1}{\left(\frac{2\pi}{L}\right)} \frac{1}{L} = g_s \frac{k}{2\pi} \quad (1.2)$$

where g_s is the degeneracy of electron spin. From Equation (1.2), the following equation is obtained.

$$\frac{\partial N}{\partial k} = \frac{g_s}{2\pi} \quad (1.3)$$

The energy E is expressed as

$$E = \frac{\hbar^2 k^2}{2m^*}$$

where \hbar is the reduced Planck constant and m^* is the effective electron mass. This equation is transformed to

$$\frac{\partial k}{\partial E} = \frac{1}{\hbar} \sqrt{\frac{m^*}{2E}} \quad (1.4)$$

By substituting Equation (1.3) and (1.4) into (1.1), 1D density of states is calculated as

$$g(E) = \frac{g_s}{2\pi\hbar} \sqrt{\frac{m^*}{2E}} \quad (1.5)$$

The current I flowing through the wire is expressed as [12]

$$I = en\delta v \quad (1.6)$$

where e is the electron charge, n is half the number of carriers per unit length, and δv is the increase of electron velocity. The number of carriers is calculated by integrating Equation (1.5).

Half of the total carriers n can then be calculated as follows

$$n = \int_0^{E_F} g(E) dE = \frac{g_s}{\pi\hbar} \sqrt{\frac{m^* E_F}{2}} = \frac{g_s m^* v_F}{2\pi\hbar} \quad (1.7)$$

where E_F is the Fermi energy and v_F is the Fermi velocity. When voltage V is applied to the wire, the increase of electron velocity is obtained from the following equation.

$$eV = \frac{1}{2} m^* (v_F + \delta v)^2 - \frac{1}{2} m^* v_F^2 = m^* v_F \delta v + \frac{1}{2} m^* \delta v^2 \approx m^* v_F \delta v \quad (1.8)$$

In Equation (1.8), it is assumed as $\delta v \ll v_F$. From Equation (1.8), δv is expressed as

$$\delta v = \frac{eV}{m^* v_F} \quad (1.9)$$

By substituting Equation (1.7) and (1.9), the current I is expressed as

$$I = \frac{g_s e^2}{2\pi\hbar} V = g_s \frac{e^2}{h} V \quad (1.10)$$

where h is the Planck constant. This gives conductance $G = g_s \frac{e^2}{h}$ ($\frac{e^2}{h} = 3.874 \times 10^{-5}$ S) and resistance $G^{-1} = \frac{h}{g_s e^2}$ ($\frac{h}{e^2} = 25.8$ k Ω). This resistance is attributed to the impedance

mismatching contact resistance. Generally, the conductance of ballistic transport is expressed by the Landauer formula [15],

$$G = g_s \frac{e^2}{h} M T \quad (1.11)$$

where M is the total number of subbands and T is the transmission probability inside the wire.

Equation (1.11) can also be written as

$$G^{-1} = \frac{h}{g_s e^2 M} \frac{1}{T} = \frac{h}{g_s e^2 M} + \frac{h}{g_s e^2 M} \frac{1-T}{T} \quad (1.12)$$

The first term is the impedance mismatch contact resistance, and the second term indicates the intrinsic resistance of the wire. In such a case that the scattering inside wire is large (electron

mean free path $\ll L$), the second term becomes dominant, and this equation gives ohm's law (see Ref. [15]).

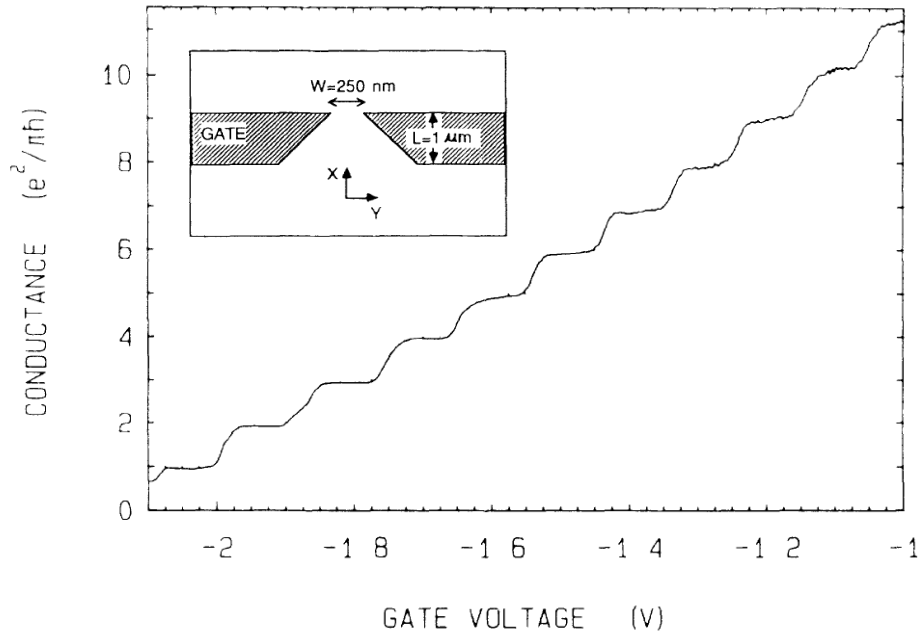


Figure 1.1: The quantized conductance of two-dimensional electron gas of GaAs-GaAlAs heterojunction with point contact structure [13].

1.2 Motivation

After the experimental discovery of graphene, two dimensional materials have obtained more attention and research effort than nanowires. Atomically thin layers can be generated from these 2D materials with weak bonds in one direction, and by applying this concept to one dimensional weakly bonded materials, single atom chains with atomic-scale diameters may be produced from those materials as illustrated in Figure 1.2. Two exemplary 1D weakly bonded materials are trigonal tellurium (Te) and selenium (Se), which have lattices consisting of spiral chains oriented along the c-axis, each spiral having three atoms per turn with adjacent chains arranged hexagonally. The chains are bound together to form a single crystal through the van der Waals force [16] or perhaps more accurately as a weakly bonded solid [17]. While there are

many 1D weakly bonded materials from which to choose, several properties of isolated Se and Te semiconductor atom chains set them apart from other 1D atomic layered materials. For example:

1. Since they are composed of a single element, an isolated Te or Se atom chain would have the smallest diameter of any known 1D material. In the case of Te, the height of the triangular spiral cross-section is 2.3 \AA , and the inter-chain distance is 3.5 \AA [18].
2. Te and Se are predicted to have direct band gaps [19, 20] of around 1 eV [21] and 2 eV [20], respectively, with strongly thickness-dependent band gaps, creating new opportunities for tiny, wavelength tunable detectors and emitters.
3. Strong light-matter interaction provided by 1D density of states and enormous exciton binding may contribute to a device which is sensitive to the dielectric constant of surrounding materials. In case of Se single atom chains, the exciton binding energy in a vacuum was simulated as 2.77 eV [20].
4. One dimensional quantum conductor of ballistic electron transport is expected due to high mobility. The Hall mobility of bulk Te was recorded as $7700 \text{ cm}^2\text{V}^{-1}\text{s}^{-1}$ at 77 K [22].
5. Strong spin-orbit coupling [23] creates an opportunity for spin-orbit qubit devices [24].

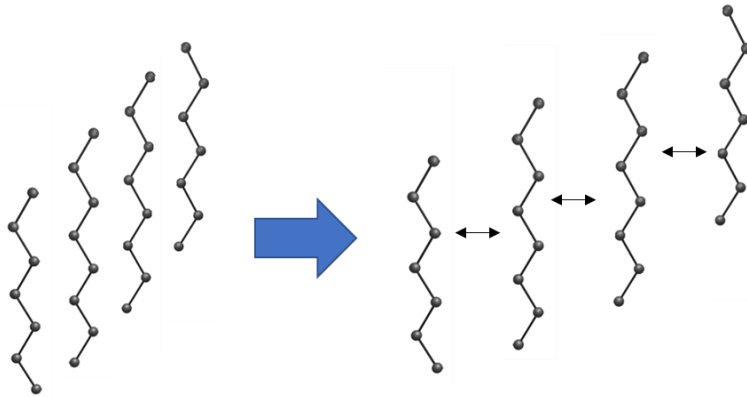


Figure 1.2: Schematic illustration of the concept of single atom chains from one dimensional weakly bonded materials.

1.2 Background about tellurium

Tellurium (Te) and selenium (Se) are group VI elements, and they have a unique crystal structure not seen in other elements. Each atom can covalently bond to one another, forming a single helical chain along the *c*-axis. These chains are weakly bonded and form a hexagonal shape in the (001) plane (Figure 1.3). It is possible to synthesize single atom chains with either element. However, we primarily focused on Te because it is known to exhibit higher mobility than Se, making it more highly suited for use in electron transport measurements; the Hall mobilities of bulk Te and Se at room temperature are $2000 \text{ cm}^2\text{V}^{-1}\text{s}^{-1}$ and $20 \text{ cm}^2\text{V}^{-1}\text{s}^{-1}$ [25], respectively.

Te is a nearly direct p-type semiconductor [26] whose bandgap was experimentally measured to be around 0.33 eV. Several methods have been proposed to obtain nanoscale Te, but the most common method for obtaining nanowires is the reduction method in a liquid phase [27-30]. In this method, certain surfactants can further encourage bonding in the *c*-axis direction by forming rod-shaped micelles that assist in unidirectional growth. The thinnest nanowire synthesized by this method had a diameter of 4-9 nm and a length of tens of micrometers [27]. Similarly, by applying different reagents, Te nanowires with 7 nm diameter were fabricated [28]. Another method commonly used is physical vapor deposition [31, 32]. Nanowires have been produced by this method on Si(111) substrates, with typical diameters of 150–200 nm at the base and 50–70 nm at the tip [31]. Another method to prepare one dimensional tellurium is utilizing zeolite pores [33, 34]. In Ref. [33], polarized Raman spectroscopy revealed that fabricated Te inside the zeolite pores was neither amorphous nor ring shaped molecules. Since one Te Raman peak was only detected along the *c*-axis of zeolite pores, it was concluded that isolated Te chains were fabricated along the *c*-axis of the zeolite pores. Atomic level Te wires have also been

demonstrated using carbon nanotubes (CNTs) [35, 36]. Vaporized Te was introduced into a CNT, and a double helix twist Te chain encapsulated inside CNT was observed by TEM [35]. In Ref. [36], a single Te atom chain was formed, and its structure was controlled from linear to zigzag by increasing the diameter of single-walled CNT.

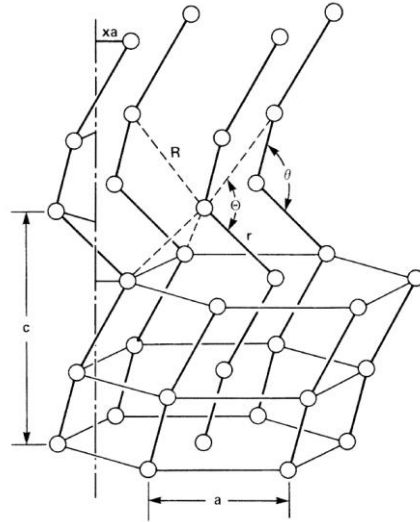


Figure 1.3: Schematic illustration of the crystal structure of Te and Se [18].

1.3 Organization

Chapter 2 covers the topographical and optical characterizations of thin flakes and ultra-thin wires fabricated by mechanical exfoliation of single crystal Te. In chapter 3, Te and Se crystal wires were grown by physical vapor deposition on SiO_2 substrates and r-plane sapphire substrates with atomic steps. In chapter 4, the Te nanowires synthesized in chapter 2 were characterized by electron transport measurements. Of the three devices successfully fabricated (device 1-JA, 1-WI, and 2-SF), device 1-JA exhibited a mobility of $1032 \text{ cm}^2\text{V}^{-1}\text{s}^{-1}$ at a temperature of 10 K, which is a promising enough result to suggest that such a device could be used for quantum transport measurements. The summary and future work of this research are described in chapter 5.

Chapter 2 Mechanical exfoliation of single crystal tellurium

2.1 Introduction

The most common method of mechanical exfoliation is the scotch tape method. In this method, half of a sticky tape is pressed onto the sample then peeled away, taking with it several layers of the sample. The other half of the tape is then pressed repeatedly to the half containing the sample, thereby exfoliating it. Thin layers of the sample are afterwards deposited onto a SiO₂ substrate by pressing the exfoliated sample-loaded tape to the substrate, then peeling it away. Another example of mechanical exfoliation method is the rubbing method. Few-layer thin flakes of graphene, hexagonal boron nitride (h-BN), molybdenum disulphide (MoS₂), and tungsten disulphide (WS₂) have been produced by rubbing their bulk powders [37]. As described in chapter 1, Te is a one dimensional weakly bonded material, but it was challenging to exfoliate by the scotch tape method because single crystal Te is a hard and fragile crystal, and because its surface is difficult to peel layers of the crystal off with tape. Therefore, we selected the rubbing method for exfoliating single crystal Te.

2.2 Mechanical exfoliation

Silicon substrates with 300 nm thermal oxide layer were sonicated in acetone and IPA solution for 3 minutes. Then, they were treated with oxygen plasma for 30 seconds to increase the adhesion of Te. Trigonal Te single crystals (Figure 2.1 (a)) were manually rubbed on the silicon substrate with the c-axis of the crystal perpendicular to the direction of the rubbing motion. Thin Te flakes were identified using contrast with an optical microscope. Thin Te flakes showed up with a progression of colors in reflected light microscopy with the thinnest crystals appearing as darker greens and blues on this silicon substrate (Figure 2.1 (b)).

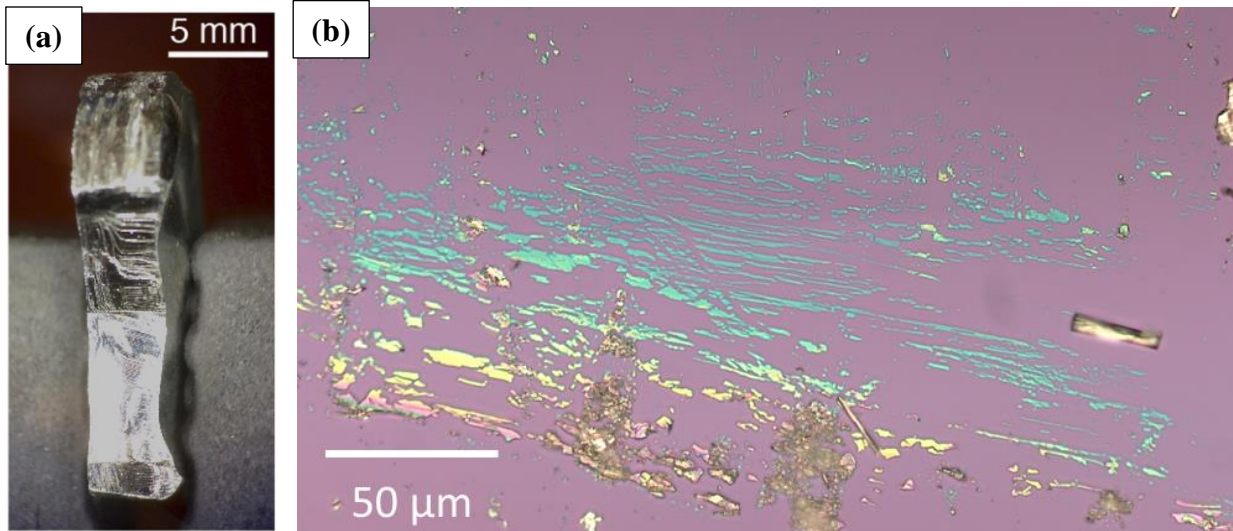


Figure 2.1: (a) Trigonal single Te crystal. (b) Optical microscopy image of mechanically exfoliated Te flakes.

2.3 Te flake

Tellurium was exfoliated in anisotropic linear bands. Atomic force microscopy of some of these bands reveals heights in the 10–15 nm range (Figure 2.1Figure 2.2 (b)), with ridges running along the length of the bands that are evident in both the height image and the height profile taken perpendicular to one of the bands as shown in Figure 2.2 (c). The modulated surface pattern and variation in wire width are evidence that the atom chains randomly break away from the bulk crystal both laterally and vertically, unlike 2D layered materials such as graphene which exfoliate with mostly flat surfaces whether a tape or sliding technique is used.

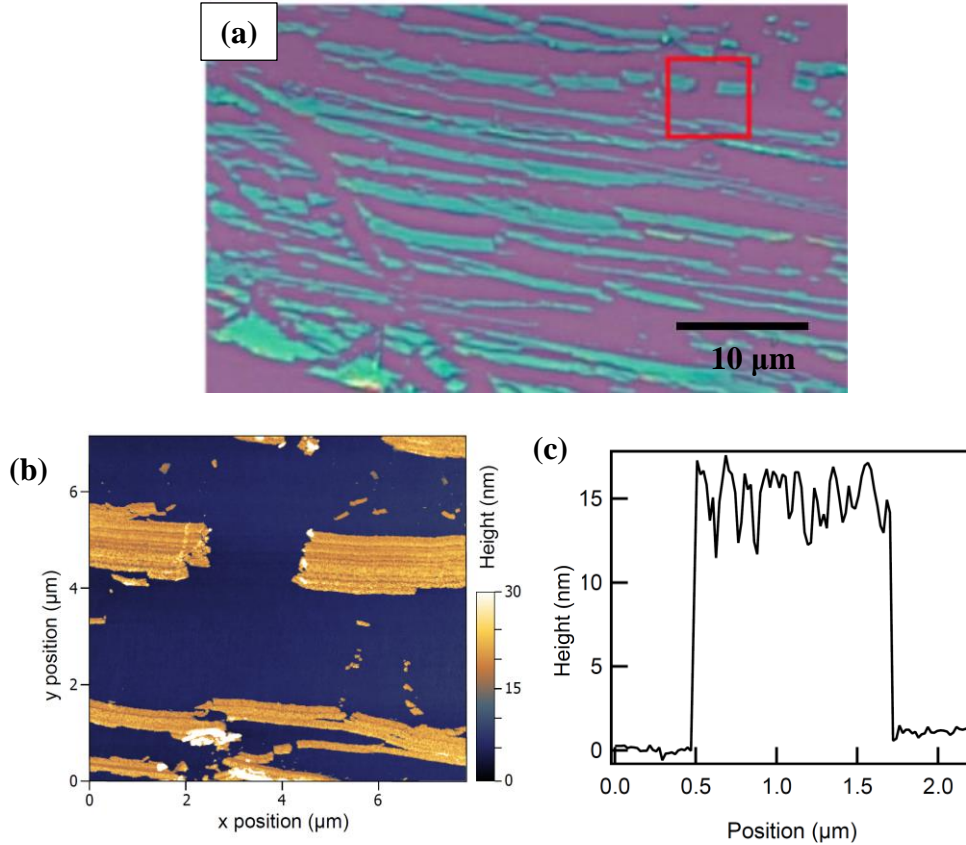


Figure 2.2: (a) Optical microscopy image of Te flakes. (b) AFM image of area indicated by the red rectangle in (a). (c) Height profile of (b).

2.4 Ultra-thin Te wire

We were able to obtain wires of 1–2 nm thickness using this sliding technique. For example, the atomic force microscope images of the second sample reveal a similar anisotropic structure of the exfoliated material (Figure 2.3 (a)), as well as significantly narrower Te nanowires with heights in the subnanometer range (Figure 2.3 (b)-(d)) or at least corresponding to two to four chains for an inter-chain distance of 3.5 \AA [18]. These ultrathin Te nanowires have lengths of 100–200 nm (Figure 2.3 (a)). A height profile taken along the c-axis direction (green line in Figure 2.3 (b), green curve in Figure 2.3 (d)) indicates that the surface roughness along the top of this 2–3 nm tall nanowire is comparable to or less than that of the SiO_2 substrate.

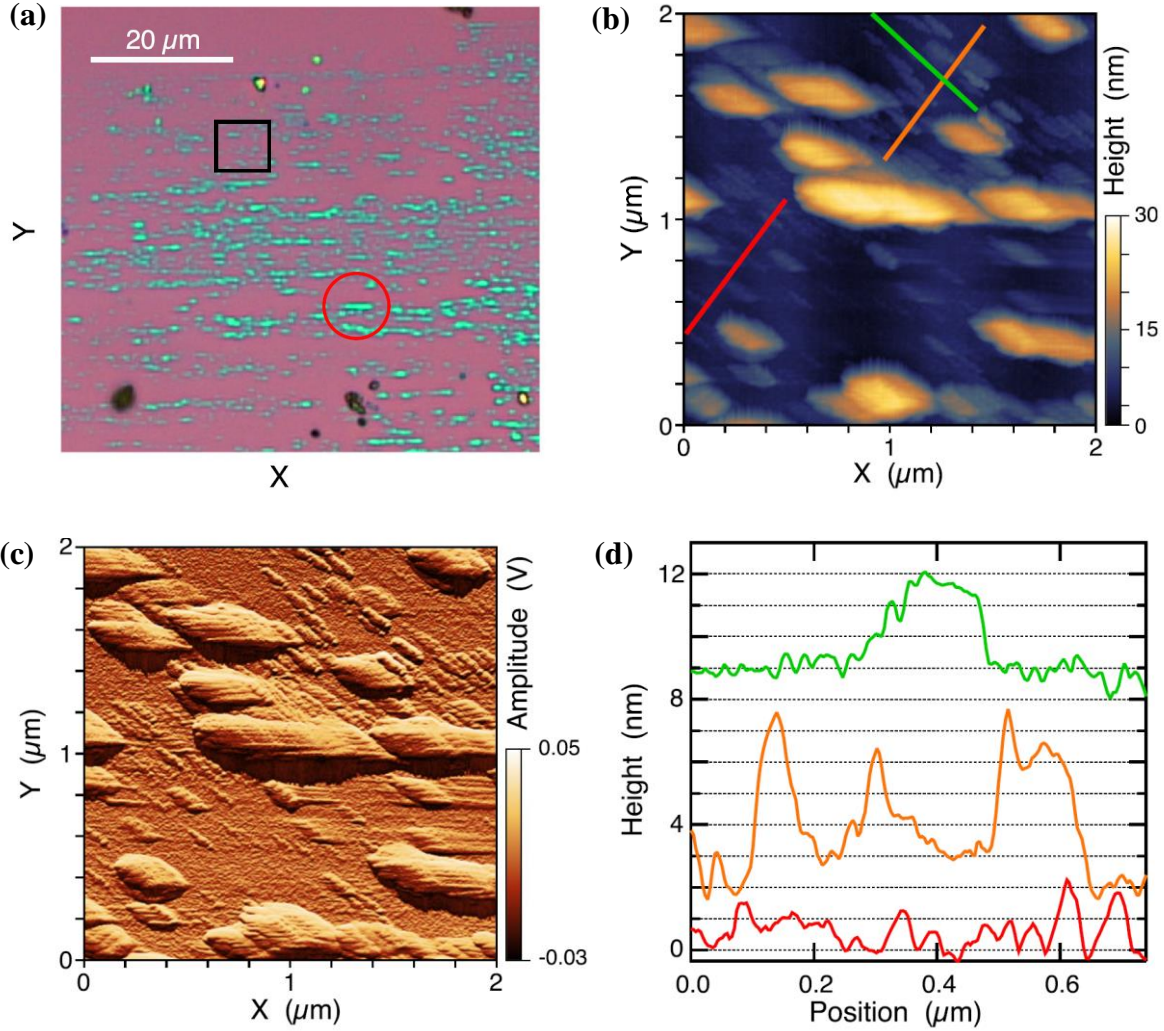


Figure 2.3: Ultra-thin wires. (a) Optical microscopy image. (b,c) AFM image. (d) Height profiles of (b).

We further characterize the exfoliated Te by Raman spectroscopy. The Raman spectrum of bulk Te at room temperature is dominated by two sets of modes: an A1 singlet at 120 cm^{-1} and a pair of E doublets at 92 (104) and 141 (141) for transverse (longitudinal) phonons [38]. The A1 and E modes of trigonal Te may be visualized as symmetric and antisymmetric breathing modes of the triangular cross-section of the Te chain [39]. This spectrum is reproduced in Figure 2.4 (a) for an excitation wavelength of 633 nm, with the lower E mode absent because of the

polarization direction of the incident light [23]. Peak positions agree with those reported in Ref. [38] to within 1 cm^{-1} .

The Raman spectrum of an approximately 30 nm thick Te flake (red circle in Figure 2.3 (a)) shows the same two peaks, shifted to slightly higher frequencies (Figure 2.4 (a)). The measured Raman peak of the silicon substrate at 520.9 cm^{-1} indicates that the spectrometer was calibrated to better than 1 cm^{-1} . Despite a slight asymmetry in the Raman peaks for both bulk and exfoliated Te, a pair of Lorentzians fits the spectra reasonably well (black curves in Figure 2.4 (a)). Peak parameters extracted from the fits indicate a mode hardening for the exfoliated flake relative to the bulk crystal of 4 cm^{-1} for the A1 mode and 2 cm^{-1} for the E mode. One interpretation of this mode hardening is a flake-substrate interaction, which can occur if the Te is strained as it is exfoliated on the SiO_2 substrate. Interaction with the substrate also generically hardens the radial breathing modes of carbon nanotubes [40]. Another possibility is that inter-chain interactions were reduced in ultra-thin Te because a significant fraction of chains is missing one or more neighbors. A naïve expectation would be that weaker inter-chain coupling would soften the A1 mode; however, applying pressure to Te crystals is known to reduce the A1 frequency [41]. Our measurement of a smaller shift for the E mode than the A1 mode (Figure 2.4 (a)) is also consistent with the pressure dependence reported in Ref. [41], but substrate-induced strain may be expected to produce similar behavior. We are unable to conclude within the scope of this work whether substrate interaction or reduced inter-chain interactions are responsible for the spectral shifts we observed.

For the sample shown in Figure 2.3, both optical and atomic force microscopy display elongated, horizontally aligned Te flakes, which suggests that the *c*-axis of the Te crystal is horizontal in these images. However, the AFM images (Figure 2.3 (b) (c)) also show that a

significant fraction of the exfoliated flakes, particularly the thinnest ones, are tilted 45° away from horizontal. To confirm the crystal orientation of this sample, we used polarization-resolved Raman spectroscopy. The polarization of the excitation beam was rotated with a half-wave plate, and the integrated Raman intensity from 85 to 170 cm^{-1} is shown in Figure 2.4 (c). The intensities were normalized by the laser power under the microscope objective measured at each polarization angle. The Raman intensity shows two maxima within one full rotation, located at 45° and 225° with respect to the X and Y axes defined in the microscope images (Figure 2.3).

Meanwhile, the optical absorption and polarizability of bulk Te at 633 nm is stronger for light polarized perpendicular to the c-axis than for parallel polarization [42]. For Te flakes with nearly bulk-like optical properties (Figure 2.4 (a)), we therefore expect Raman intensity to be higher for light polarized perpendicular to the c-axis. Based on the angle of the Raman maximum in Figure 2.4 (c), we concluded that the Te nanowires oriented at 45° in Figure 2.3 (c) were elongated parallel to the c-axis for that sample. Because different Te flakes on the same substrate were used for Raman spectroscopy and AFM, an assumption of this conclusion is that the crystal axes are the same for all exfoliated flakes shown in Figure 2.3 (a). This assumption would not be appropriate for flakes prepared by the traditional tape exfoliation method, but it is a reasonable assumption for the unidirectional rubbing technique used here. These observations demonstrated that polarized Raman spectroscopy is sufficient to determine the crystal orientation of nanoscale exfoliated Te. This technique is useful in practice given that optical and atomic force microscopy do not provide unambiguous information about crystal orientation.

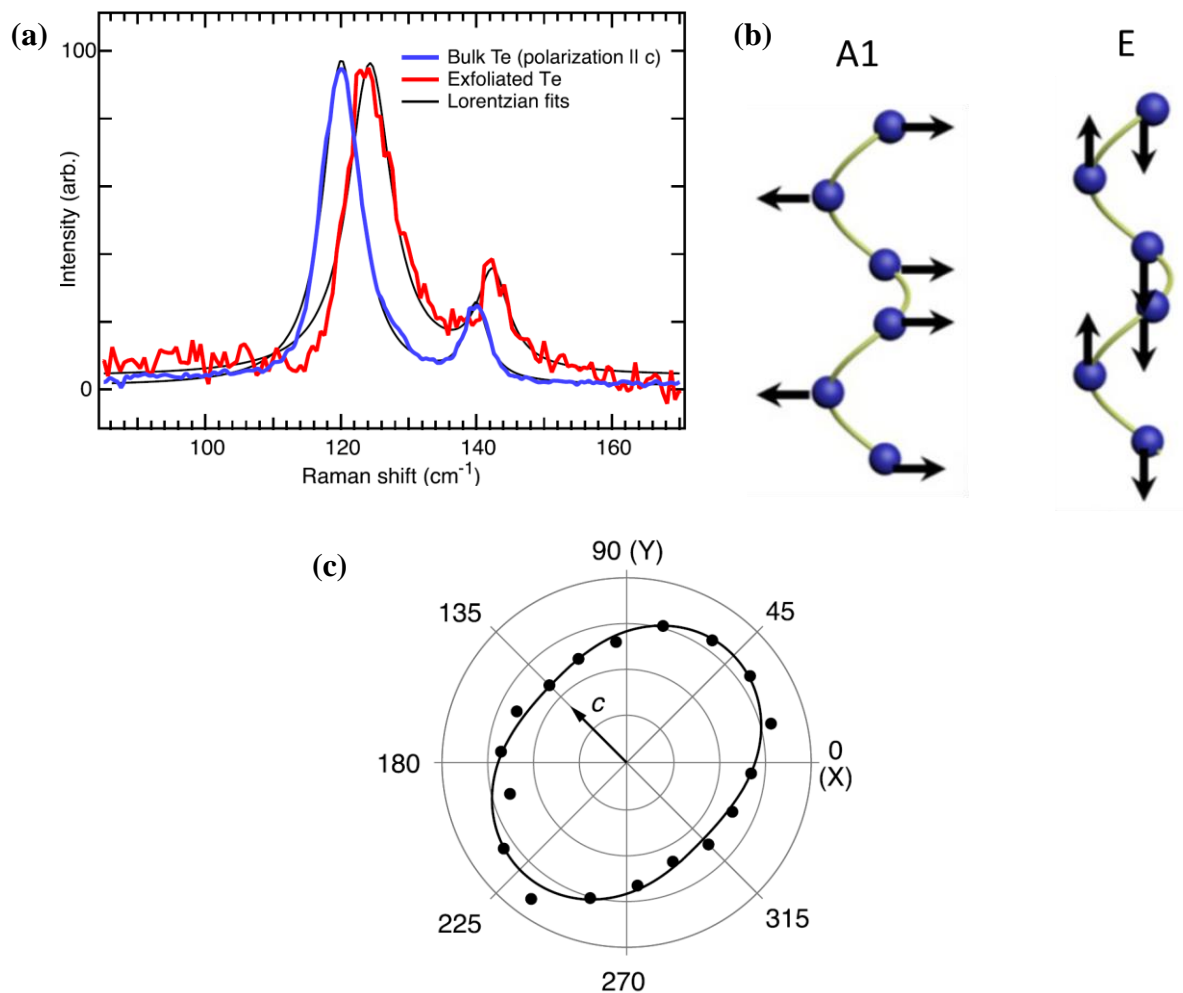


Figure 2.4: Polarized Raman spectroscopy of ultra-thin Te wire. (a) Polarized Raman spectra of bulk and ultra-thin wire under the same excitation condition (633nm, polarization parallel to c-axis). (b) Raman mode diagram in Ref. [23]. (c) Polar plot of Raman intensity averaged over the spectral range in (a).

2.5 Oxygen plasma effect on tellurium flakes

2.5.1 Height of Te flake

Oxygen plasma can be used for etching thin flakes of materials. For example, it has been used to decrease the thickness of graphene from two layers to one layer [43]. We applied this technique to fabricate the thin Te flakes described in §2.2. Figure 2.5 (f) shows a decrease in the height of the flake with increasing oxygen plasma exposure time. Figure 2.5 (g) is the

relationship between average height of (f) and oxygen plasma exposure time. The slope of (g) is notably not linear at the beginning of the plasma exposure. Another interesting phenomenon that occurred when this method was applied was the change in the surface structure of the flake. As the plasma exposure time increased, holes steadily appeared on the flake surface. This can be attributed to the thought that defects originally located on the Te flake surface were highly susceptible to reacting with the plasma.

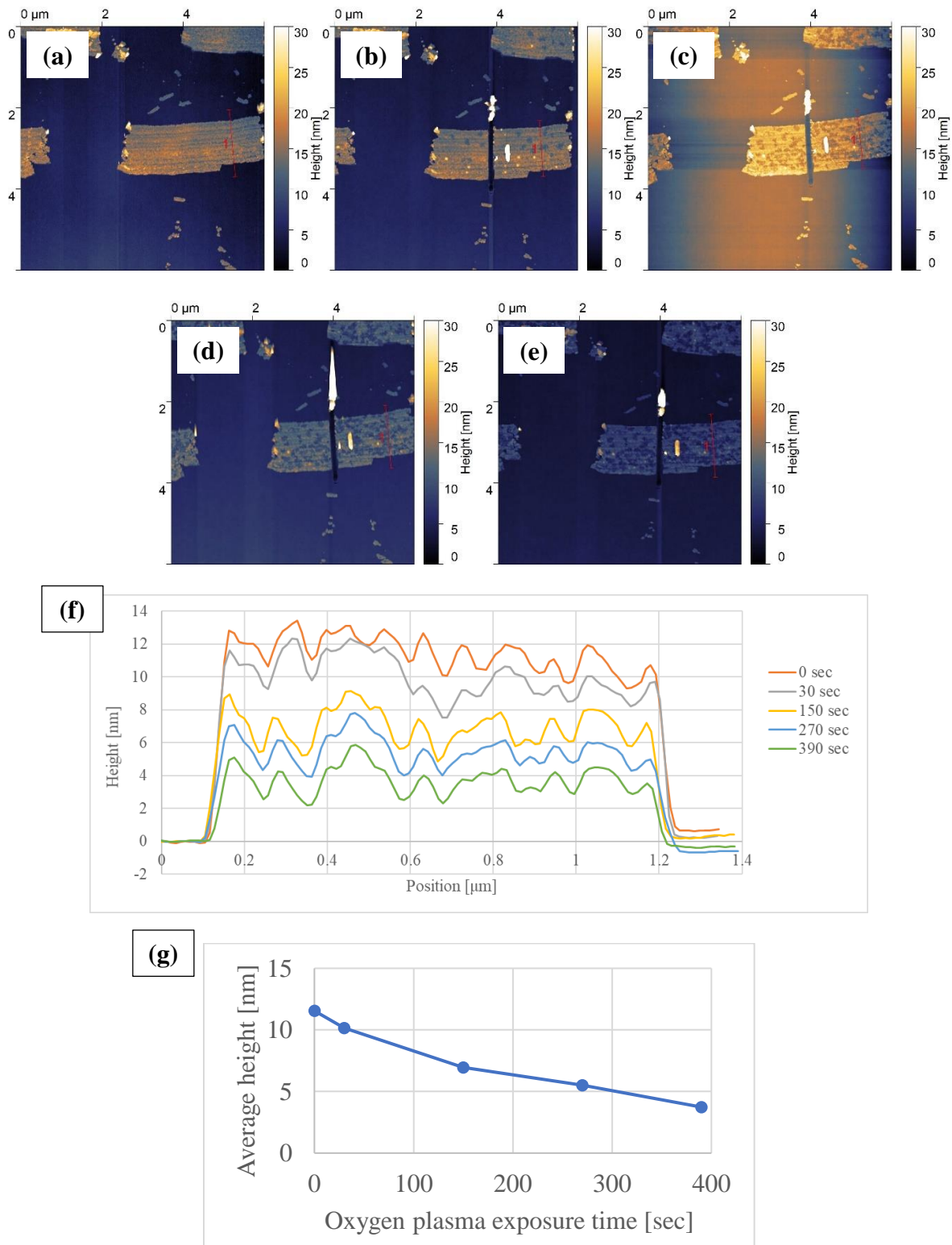


Figure 2.5: AFM images after oxygen plasma etching for (a) 0 sec (b) 30 sec (c) 150 sec (d) 270 sec (e) 390 sec. (f) Height profile of (a-e). (g) Average height in (f) vs oxygen plasma exposure time.

2.5.2 Raman intensity

After performing plasma etching, there were no Te peaks visible in the Raman spectra. This may have been because the intensity of the oxygen plasma treatment might have affected the Te crystal structure. In order to confirm this theory, an experiment was design to observe the relationship between the plasma etching technique and the resulting Raman Te peaks. Table 2.1 shows the oxygen plasma treatment conditions. Figure 2.6 (a) and (b) are the optical images before and after the 5th plasma treatment, and (c-e) are the Raman intensity changes after plasma treatment of flakes 1–3 indicated in (a), respectively. The Raman spectra for each Te flake were normalized to the silicon Raman peak at 520.9 cm^{-1} , which was taken on the same SiO_2 substrate away from any Te flakes in order to avoid the relative Raman peak intensity of Si to Te becoming larger due to the thickness decrease of Te flakes after oxygen plasma treatment. From (a) and (b), it can be seen that there is no significant flake color difference before and after oxygen plasma. However, from (c) and (d), it is apparent that the Te Raman peak intensity decreased each time plasma etching was performed after the first time. In the case of (e), the Te peak completely disappeared after the 4th plasma treatment. From these results, it seems likely that the decrease of the Te Raman peak can be attributed to the destruction of the Te crystal structure, or more simply to the decrease in the amount of Te.

Table 2.1: Oxygen plasma treatment condition

O2 plasma treatment	Pressure	Power	Time
	[mtorr]	[W]	[s]
1 st	75	75	60
2 nd	75	75	120
3 rd	50	75	2
4 th	50	75	20
5 th	50	75	120

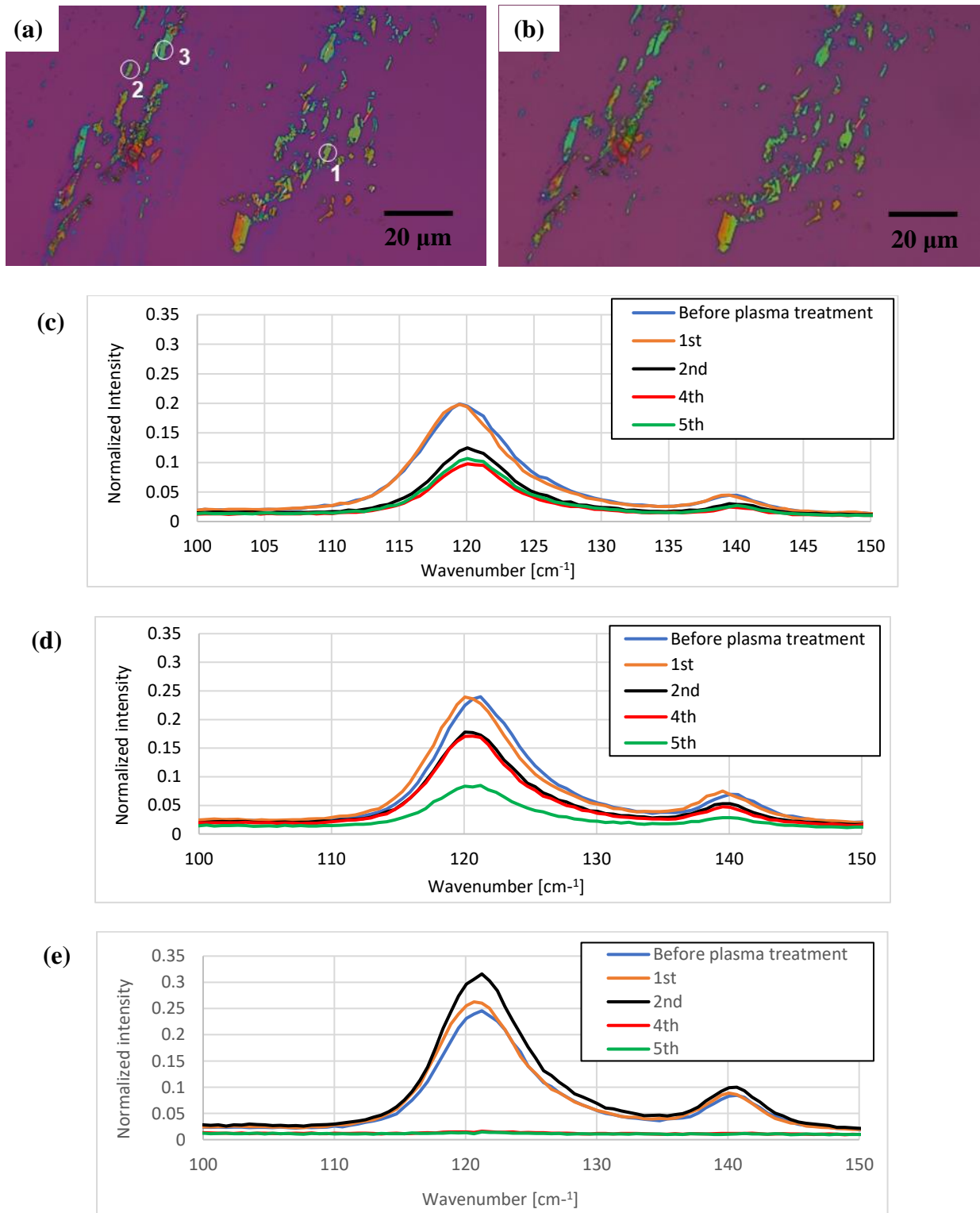


Figure 2.6: Optical images of (a) before and (b) after 5th plasma treatment. (c-e) Raman spectra change after oxygen plasma treatment for each flake indicated in (a). All Raman spectra were normalized by using silicon peak at 520 cm⁻¹ measured on the same SiO₂ substrate away from any Te flakes.

2.6 The challenge of Te exfoliation

Exfoliated Te flakes and wires are discussed in §2.2-2.4, focusing particularly on optical and structural characteristics. An important measurement with regards to Te flakes and wires is their electrical characterization, which we need materials of a relatively large lateral size (at least 3–4 μm) in order to make metal contacts on them for performing electrical measurements. However, the probability of obtaining such thin flakes and wires was quite low. In most cases, only large crystal fragments with heights around 1 μm could be exfoliated. Although blue colored Te was fabricated by exfoliation, those materials were too small to make contacts on them for performing transport measurements. Therefore, mechanical exfoliation was not an effective method for preparing a transport measurement sample.

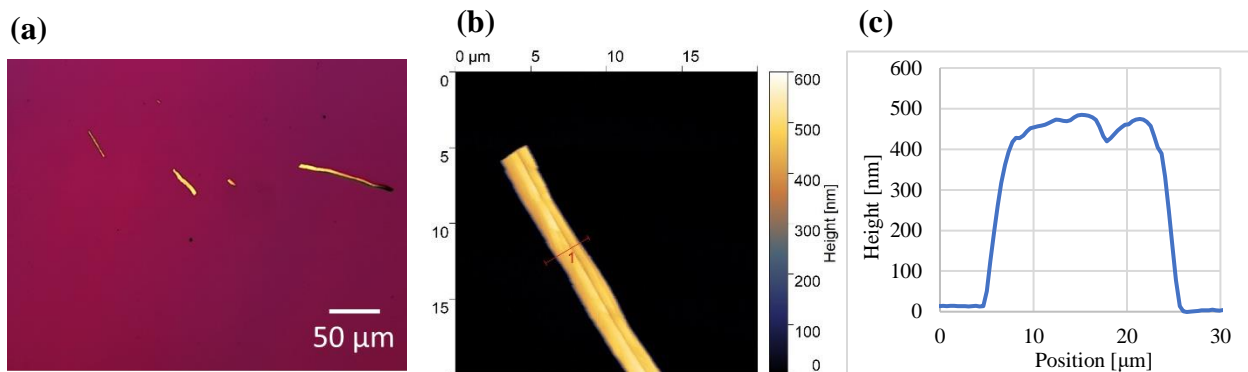


Figure 2.7: (a) Optical image, (b) AFM image and (c) height profile of bulk Te after mechanical exfoliation.



Figure 2.8: Optical image of small particle Te after exfoliation.

Chapter 3 Physical vapor deposition of tellurium and selenium

3.1 Introduction

One of the methods for fabricating ultra-thin nanowires is using a substrate whose surface structure consists of atomic steps. Xiao et al. controlled the growth direction of single-walled carbon nanotubes using Y and Z-ST cut quartz by chemical vapor deposition (CVD) [44]. In Ref. [45], MoS₂, which is a common 2D material, formed nanowires with 0.65 nm wire radius on an Au(111) surface by molecular beam epitaxy (MBE), and it was confirmed that those wires consisted of three atom chains by high-resolution NC-AFM. In addition to these experiment results using atomic step substrates, it is known that Te and Se tend to grow along their chain directions due to their anisotropic crystal structures. Because of this characteristic, the growth of Te and Se on atomic step substrates was hypothesized as a possible method for the synthesis of single atom chains. First, we focused on physical vapor deposition for Te and Se growth since this method is quite simple and less costly compared to CVD and MBE. To hunt for fabricated wires, we tried photoluminescence imaging technique, which is a technique commonly applied to capture images of carbon nanotubes [46, 47].

3.2 Physical vapor deposition on SiO₂ substrates

Te and Se were grown by using a two-zone furnace (Figure 3.1) as described in Ref. [48]. An amorphous Te or Se pellet and silicon substrate were each put on a boat, and those boats were placed inside a quartz tube 20 cm apart from each other. Prior to growth, silicon substrates were sonicated in acetone and IPA. During growth, argon (Ar) gas was flowing from the seed side to the silicon substrate side. To assist the Ar gas flow and prevent oxidation during growth,

a vacuum was drawn in the quartz tube by a vacuum pump. Physical vapor deposition was primarily conducted by Rabindra Basnet and Krishna Pandey from Dr. Jin Hu's laboratory.

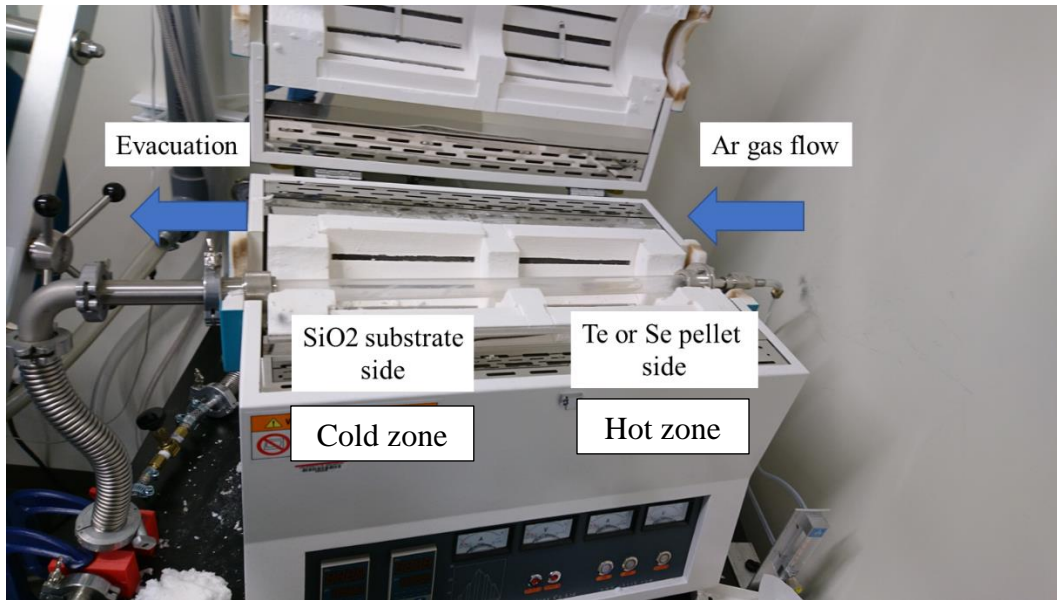


Figure 3.1: Image of physical vapor deposition set-up.

3.3 Characterization of deposited tellurium and selenium

3.3.1 Tellurium

Physical vapor deposition of Te has been reported in several articles [49] [31] [32], and the formation of Te wires was observed. Because of the anisotropic crystal structure of Te, these wires tend to grow along the c-axis, and this has been confirmed in other articles by XRD [31] and TEM [32]. Figure 3.2 shows two examples of optical images after Te wires were grown on an SiO₂ substrate with seed temperatures of 450 and 500 °C. The deposition side temperature was set to 200 °C in each case. Through several growth experiments with different growth conditions, it was revealed that the thickness of the Te wire generally increased with increasing seed side temperature. From Figure 3.2, it is apparent that the height of these wires is in the order of μm or greater. In order to perform transport measurements, metal contacts need to be

fabricated so that there is no short or discontinuity. These samples were not suitable due to the high density of wires on the substrate and the relatively large height of wires. Wires were transported using tape (ULTRON SYSTEMS, 1009R-6.0) onto a new SiO₂ substrate. This tape is less sticky than scotch tape, so an adequate amount of Te could be transferred onto a SiO₂ substrate. Figure 3.3 (a) illustrates the transported flakes and wires from Figure 3.2 (a) substrate, and Figure 3.3 (b) and (d) are AFM images of the flake and the wire indicated by the black circles in (a). From the AFM images, the height of both wire and flake were around 70 nm. We also characterized the flake by polarized Raman spectroscopy. From Figure 3.4, the x direction is determined as the c-axis because of the absence of the 92 cm⁻¹ peak. Also, three Te peaks indicate that the fabricated Te was not amorphous but crystalline.

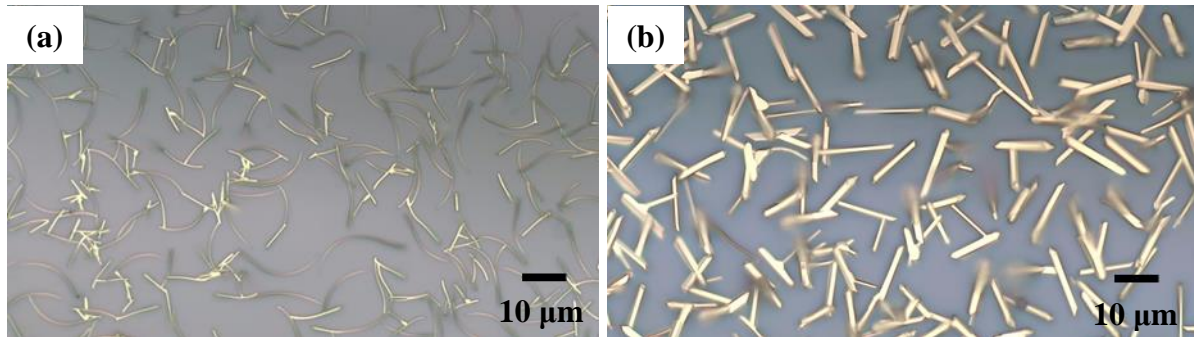


Figure 3.2: Optical microscopy image of Te after physical vapor deposition with the seed side temperature of (a) 450 °C and (b) 500 °C.

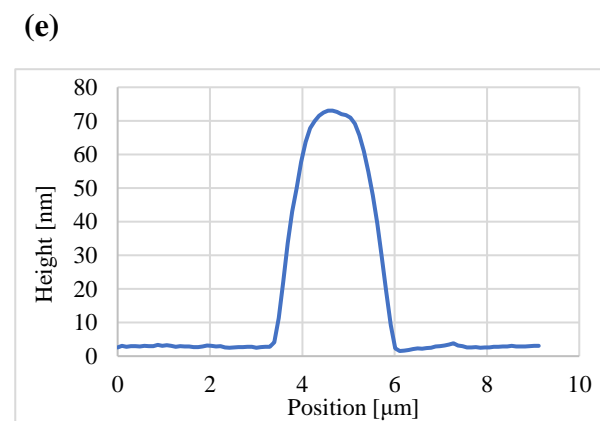
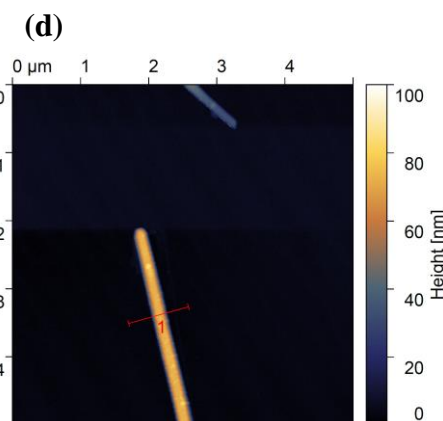
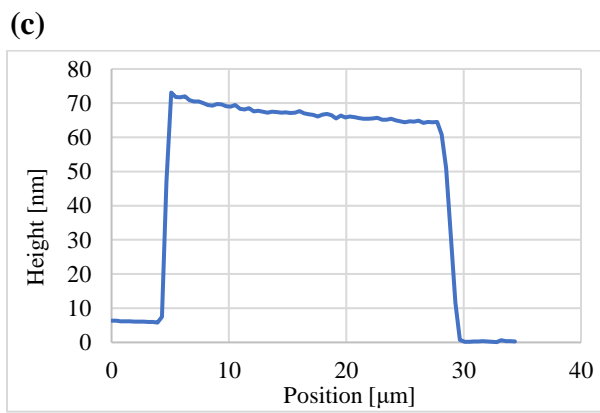
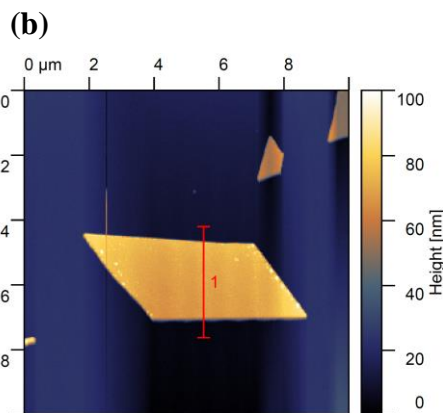
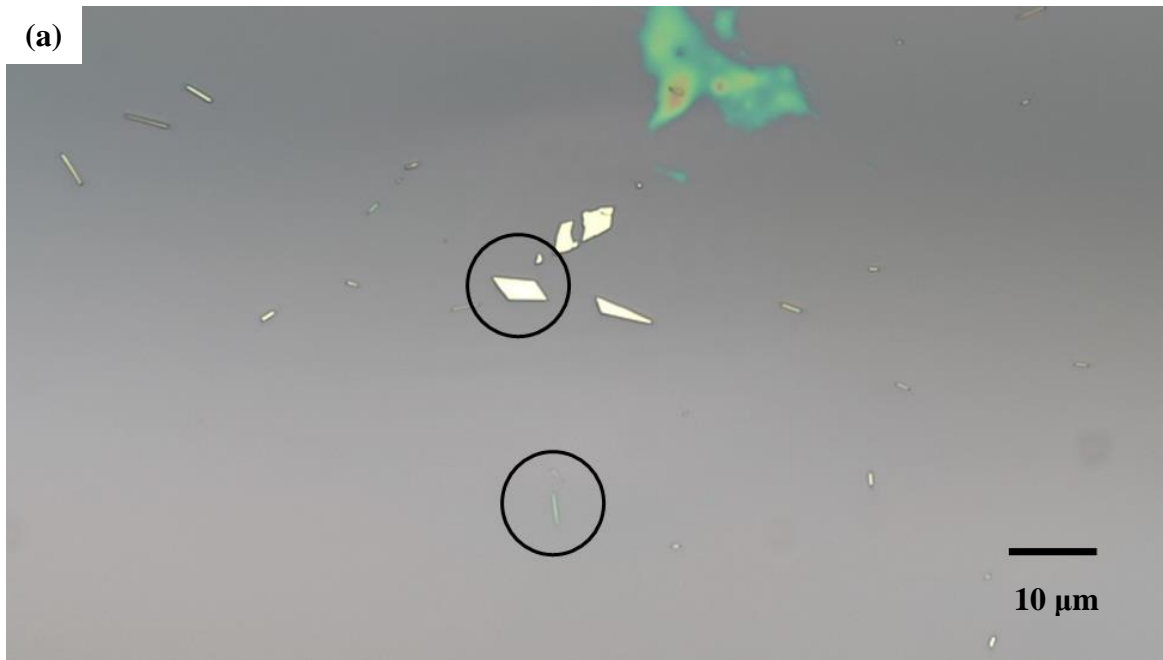


Figure 3.3: (a) Optical microscopy image after transport of grown Te onto another SiO₂ substrate. (b) AFM image of the flake in (a). (c) Height profile of (b). (d) AFM image of the wire in (a). (e) Height profile of (d).

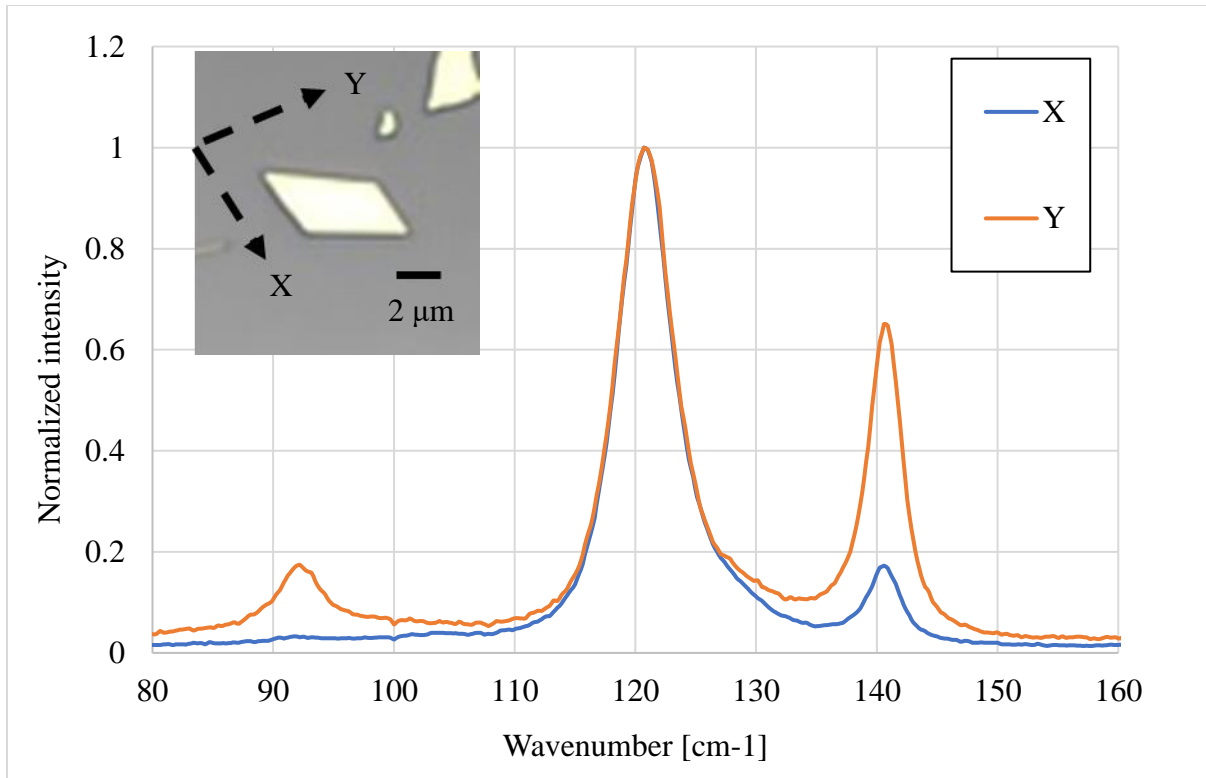


Figure 3.4: Polarized Raman spectra of the flake in Figure 3.3 (b). Inset image is the optical image of the flake.

Figure 3.5 shows the optical image about Te nanowires transferred onto another SiO_2 substrate after growth. The growth condition was same with the Figure 3.2 (a) (seed side temperature: 450°C). Compared with Figure 3.2 (a), almost all wires show the blue color, and the height of the wires were around 30 nm. Through the entire experiments, this sample exhibited the lowest height wires.

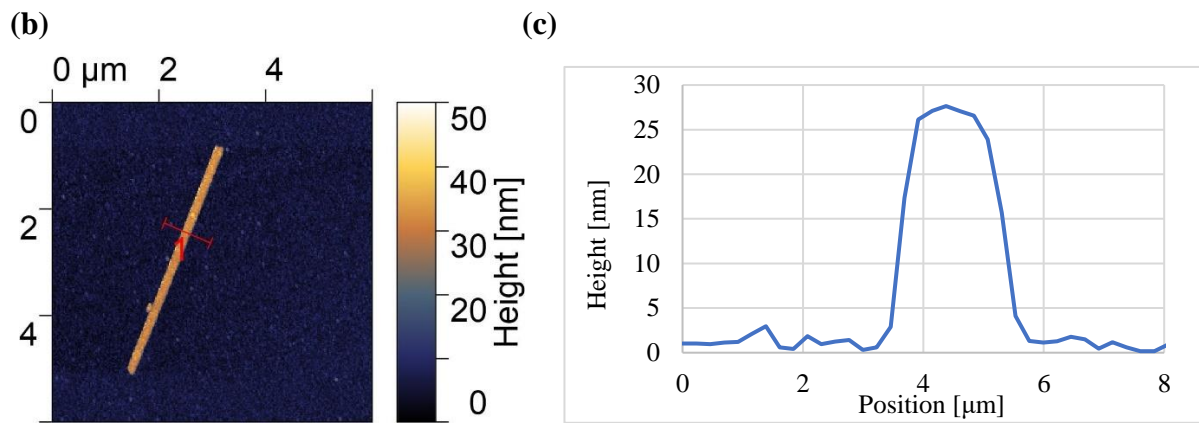


Figure 3.5: (a) Optical image of Te nanowires transferred onto another SiO_2 substrate after growth. (b) AFM image of the wire indicated in a black circle in (a). (c) Height profile of (b).

3.3.2 Selenium

Figure 3.6 (a) is the optical image after Se deposition which was carried out using Table 3.1 growth conditions. In Figure 3.6 (a), there are red colored particles and green colored wires. Figure 3.6 (b) is the Raman spectra overlay of a red colored particle and a green colored wire. The wire has a peak at 230 cm^{-1} which corresponds to the crystalline peak, and the particle has a broad peak at 250 cm^{-1} which corresponds to the amorphous peak [50]. Regarding the structure of Se, many wires seed from the green colored particles. This growth mechanism of physical vapor deposition of Se is discussed in Ref. [49]. The structure change was observed at different temperatures, and it can be concluded that the formation of amorphous Se particles is followed by the growth of crystalline Se wires. The photoluminescence spectrum of a Se wire was also measured (Figure 3.6 (c)). This spectrum has a broad peak at around 700 cm^{-1} which matches that of the Se wires in Ref. [51].

Table 3.1: Growth condition of Figure 3.6 (a)

Temperature		Growth time [minutes]	Pressure [torr]	Ar flow rate [l/min]
Seed side [°C]	Deposition side [°C]			
300	100	60	10	0.2

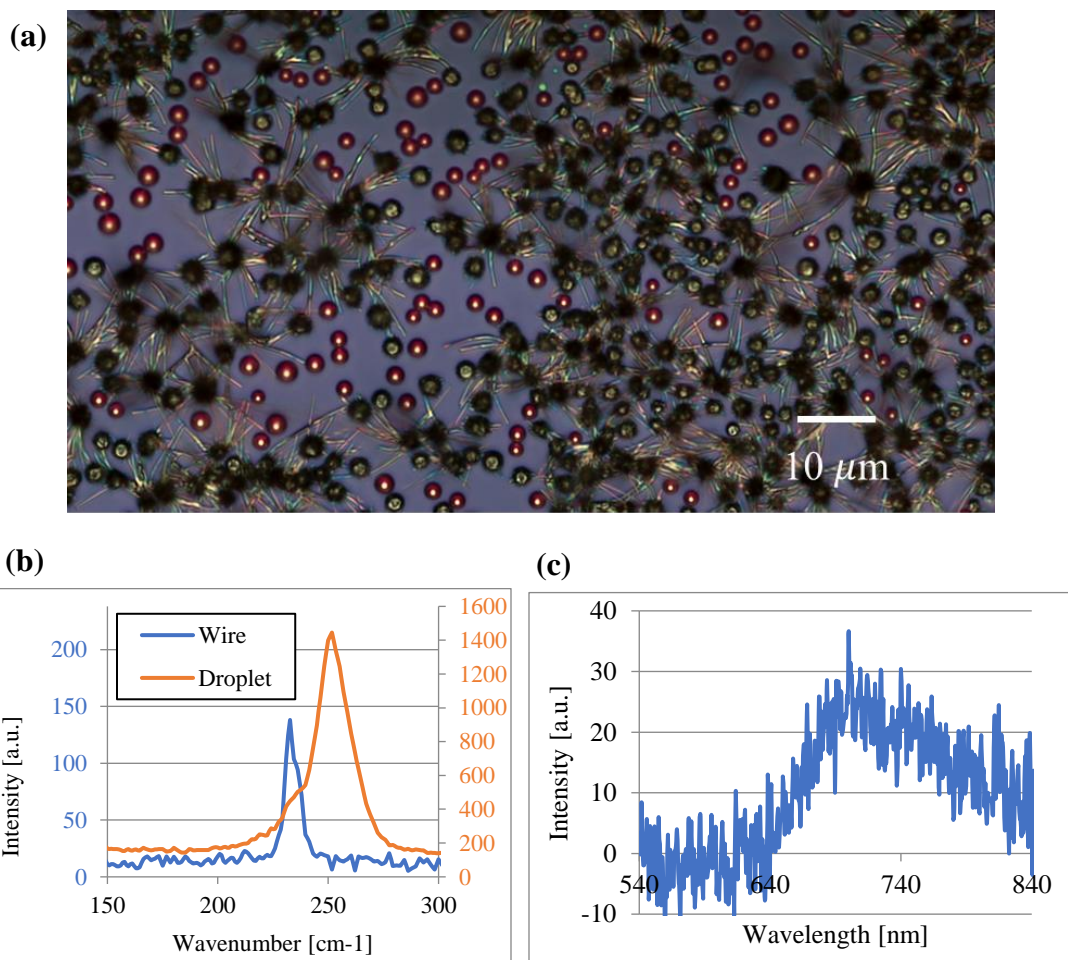


Figure 3.6: (a) Optical image after Se deposition. (b) Raman spectra of a wire and particle in (a). (c) PL spectra of a wire in (a).

The deposited Se were exfoliated by the scotch tape method. Figure 3.7 (a) is the exfoliated Se on a SiO₂ substrate, and Figure 3.7 (b) and (c) are the AFM measurement results for the two flakes indicated by the red and black circles. Regarding the AFM image of Figure 3.7 (b), the left side of the flake was burned by the laser beam. The minimum flake height achieved for Te was around 60 nm, but for Se it was noticeably lower, as can be seen in Figure 3.7. This indicates that mechanical exfoliation is more effective for Se than Te. This difference derives from the anisotropy ratio of intra-chain and inter-chain bond strength. Since Se shows more anisotropic characteristics than Te, this facilitates the production of thinner Se flakes [17].

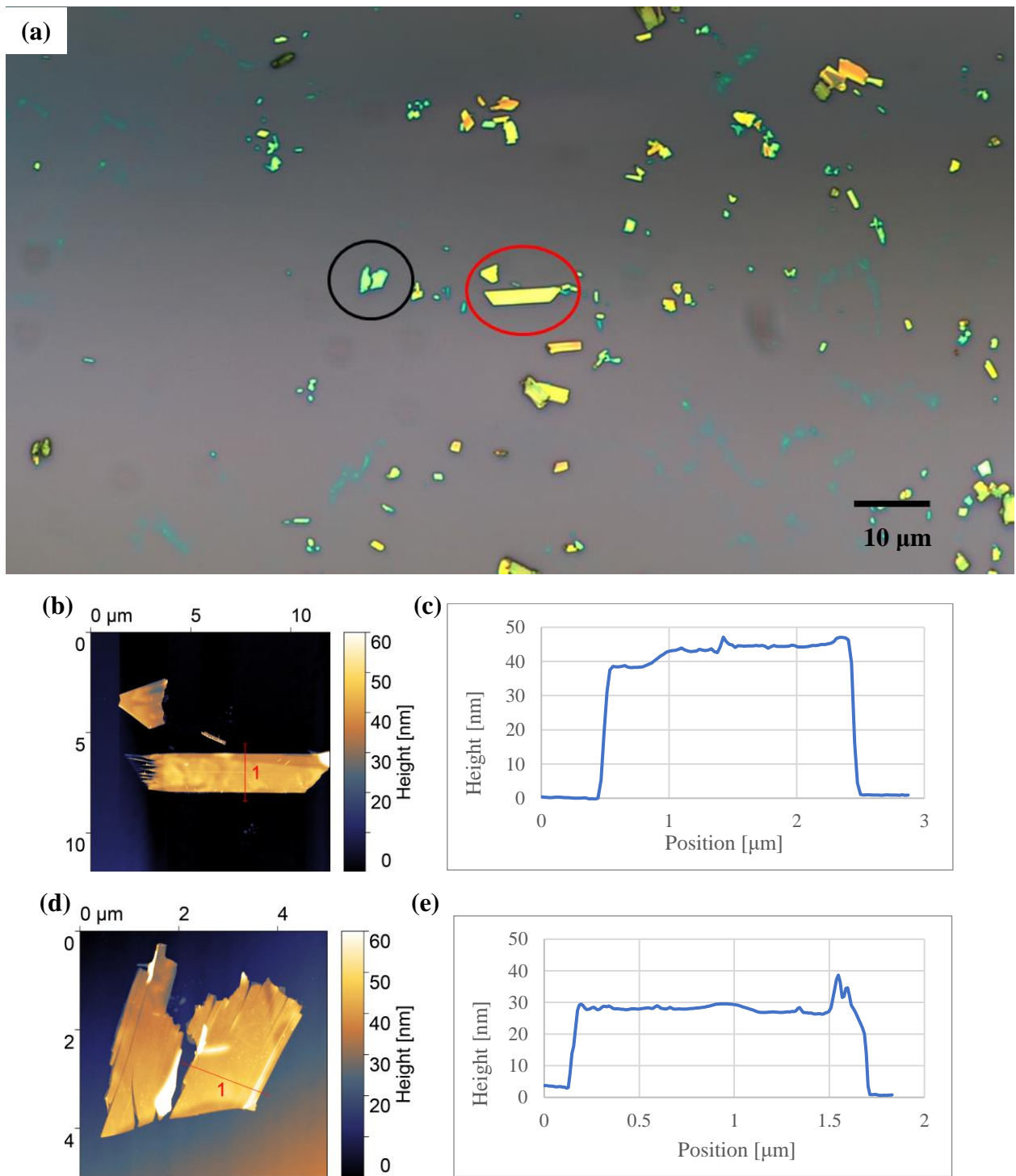


Figure 3.7: (a) Optical image of exfoliated Se. (b) AFM image of Se flake shown in a red circle in (a). (c) Height profile of (b). (d) AFM image of Se flake shown in a black circle in (a). (e) Height profile of (d).

3.4 Annealing of r-plane sapphire substrates

As described in §3.1, atomic step substrates can be used to achieve thin wire fabrication where the wires are aligned in the direction of the atomic steps. To obtain thin wires aligned with atomic steps, we focused on using r-plane sapphire as a platform for thin wire growth. By annealing a sapphire substrate at around 1000 °C, each atom tends to move into its most stable position, and this results in an atomic step-like structure. Step width can be determined by the angle misalignment achieved by cutting the sapphire along a certain plane, and step height is related to the inter-plane distance. A 2-inch r-plane sapphire substrate was cut into 5×6 mm pieces and sonicated in acetone and IPA. Then, each piece of sapphire substrate was put into a crucible, and the crucible was covered by a lid so that the insulator material inside the furnace did not fall onto the sapphire substrate. Sapphire substrates were annealed for 3 hours at different annealing temperatures. Figure 3.9 shows the AFM images before and after annealing. Before the annealing, there were a lot of small dots on the substrate, but these were gone after annealing at each temperature. After 900 and 1000 °C annealing, the atomic steps of sapphire were observed, but each step was wave shaped. At 1100 °C, each atomic step was a straight line, and the step height was around 0.4 nm. According to Ref. [52], the inter-plane distance can be calculated by Equation (3.1).

$$d_{hkl} = \frac{1}{\sqrt{\frac{4}{3a^2} (h^2 + k^2 + hk) + \frac{l^2}{c^2}}} \quad (3.1)$$

In the case of r-plane sapphire, the plane is expressed as $[1\bar{1}02]$, with lattice parameters $a=4.76 \text{ \AA}$ and $c= 12.99 \text{ \AA}$. Thus, the inter-plane distance was calculated as 3.48 \AA . This calculated distance is quite close to the experimental results, where step width was measured at

around 4 μm . From this result, the r-plane sapphire annealed at 1100 $^{\circ}\text{C}$ was used for Te atom chain growth.

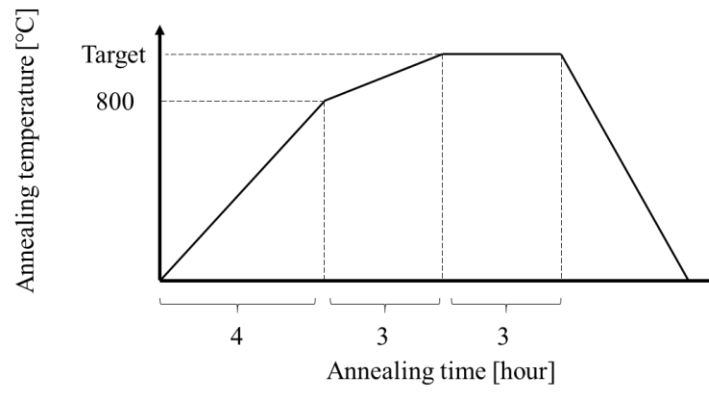


Figure 3.8: Annealing profile.

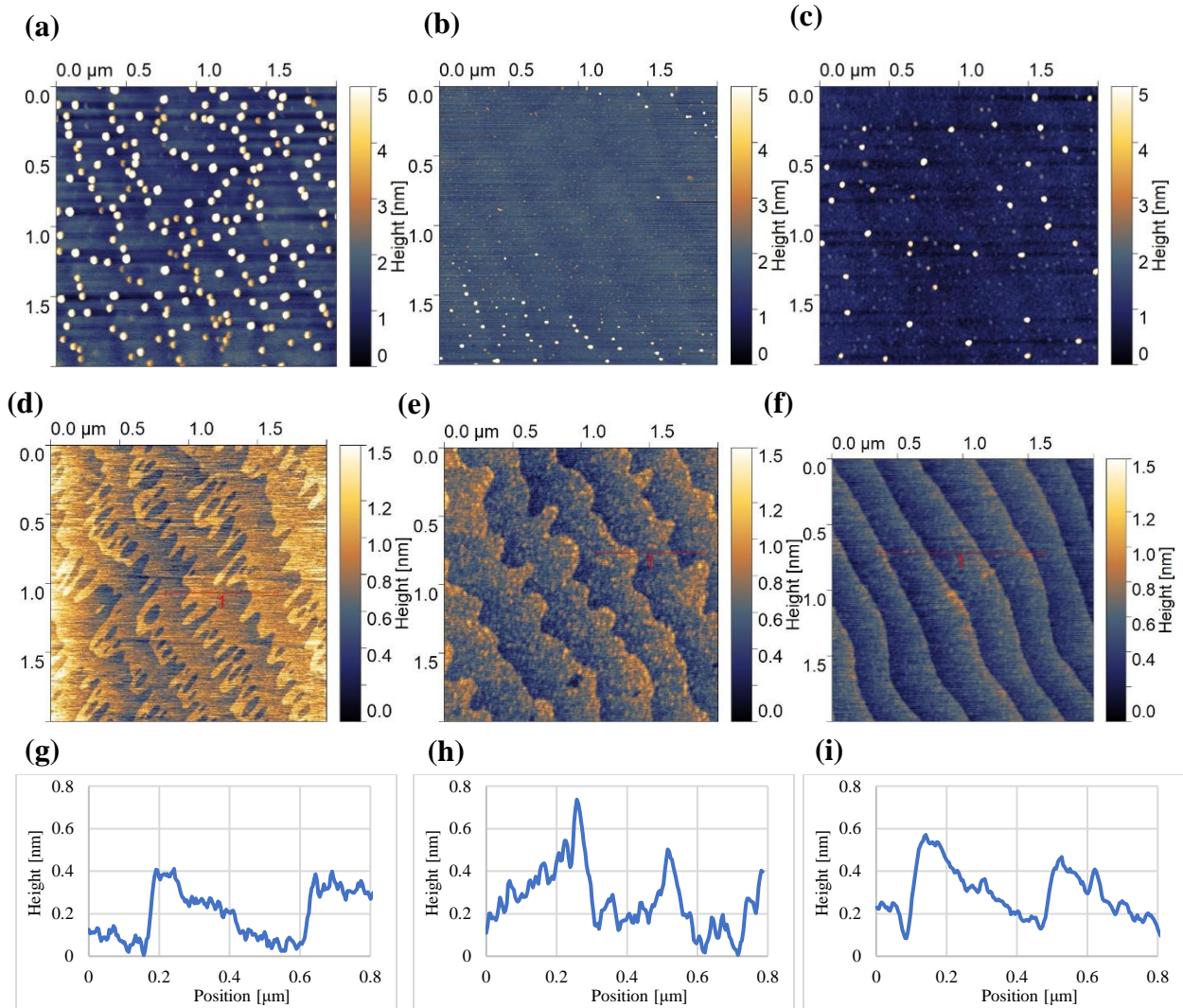


Figure 3.9: AFM image and height profile before (a-c) and after annealing for 3 hours at (d) 900 (e) 1000 (f) 1100 °C. (g-i) are the height profiles for each substrate (d-f).

3.5 Physical vapor deposition on atomic step substrates

An annealed sapphire substrate prepared as described in §3.4 was set in a quartz tube with the atomic steps aligning with the direction of Ar gas flow. To avoid oxidation of Te and Se surfaces, the grown sample substrates were immediately transferred into a glove box to protect from air exposure. During microscope observation, the sample was placed in a small box filled with Ar gas and with a thin cover glass for microscope observation (Figure 3.10). To identify the small Te and Se wires which were not observable using bright and dark field imaging, photoluminescence (PL) imaging was employed. A wavelength of 450 nm of LED was used as the light source for PL imaging. The band gap of bulk Te is 0.3 eV, but this gap increases with decreasing thickness of the Te material. According to Ref. [21], the band gap increase was revealed experimentally to be as high as 0.92 eV for monolayer Te. By decreasing the thickness of Te, the band gap changes from a nearly direct band gap to a direct band gap [19]. Meanwhile, the PL wavelength of Se was observed at around 700 nm in §3.4, and this corresponds to a band gap of 1.77 eV. In addition, the band gap of a Se atom chain has been simulated as 2.7 eV [20]. Because of these facts, we hypothesized there was a chance that thin Te and Se wires could be observed using PL imaging. We looked for thin wires which were visible in PL imaging mode and not visible in bright field mode. We checked for both Te and Se after deposition on an atomic step substrate.

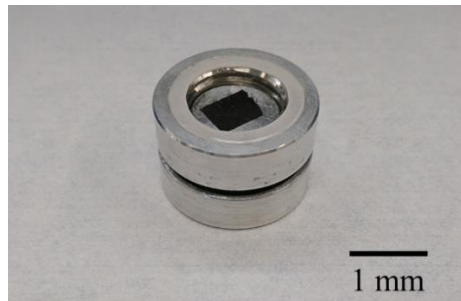


Figure 3.10: Argon gas filled box for optical microscope imaging.

Table 3.2 lists the growth conditions, and all growths were conducted on annealed sapphire substrates. Figure 3.11 (a) is the optical image of Te wires grown by No.8 growth conditions listed in Table 3.2. In Figure 3.11 (a), large Te wires are observed to have been deposited with random growth directions. Figure 3.11 (b) shows the PL mode image of the same sample. From this figure, no emissions were observed except for those produced by the sapphire substrate. Several of the growth conditions listed in Table 3.2 were attempted, but PL emissions from Te were not observed. Table 3.3 indicates the growth condition of Se on a sapphire substrate. Similarly, there is no significant differences for Se growth between SiO₂ substrate and atomic step substrate.

Table 3.2: Growth condition of Te on a r-plane sapphire substrate

No.	Temperature		Growth time [minutes]	Pressure [torr]	Ar flow rate [l/min]
	Seed side [°C]	Deposition side [°C]			
1	450	180	30	2.4	0.2
2	450	0	30	48.7	0.2
3	450	100	15	48	0.3
4	450	180	60	10	0.2
5	450	0	15	49	0.2
6	550	350	30	35	0.5
7	450	0	15	45	0.3
8	450	180	30	10	0.3
9	450	180	60	10	0.2
10	450	100	15	50	0.3
11	450	180	80	1.5	0.2
12	450	0	30	45.5	0.2
13	400	150	60	10	0.2

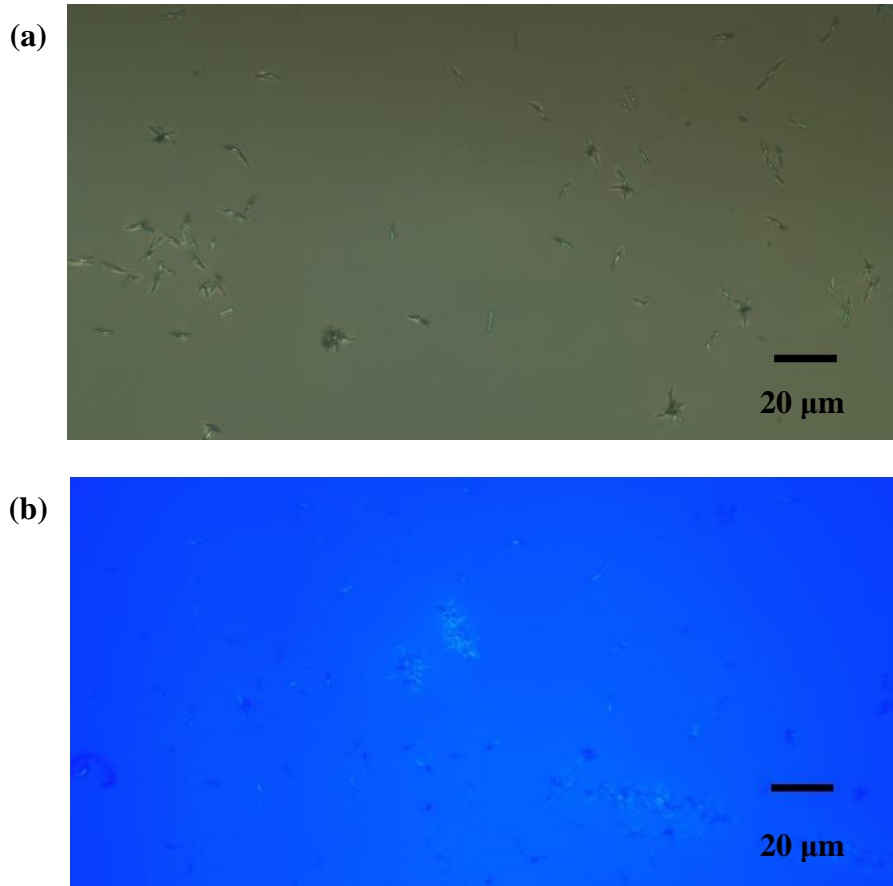


Figure 3.11: Optical image after PVD deposition of Te. (a) Bright field image. (b) PL mode image.

Table 3.3:Growth condition of Se on a r-plane sapphire substrate

No.	Temperature		Growth time [minutes]	Pressure [torr]	Ar flow rate [l/min]
	Seed side [°C]	Deposition side [°C]			
1	300	150	60	45	0.4
2	320	200	60	50	0.5
3	350	150	60	10	0.8
4	350	150	60	40	0.3
5	300	100	60	10	0.2
6	300	130	30	50	0.2
7	350	150	60	2	1
8	300	100	30	10	1
9	300	100	60	100	0.2
10	300	250	60	10	0.4
11	350	150	60	2	0.5
12	250	100	60	2	0.2
13	350	100	60	7.5	0.2

Chapter 4 Transport measurement of Te wire

4.1 Introduction

Devices composed of Te flakes or wires have been emerging rapidly. Zhou et al. fabricated Te wire field-effect transistors [53], and Wang et al. demonstrated the manufacturing of Te flake field-effect transistors [26]. In Ref. [26], the field effect mobility of Te flakes was recorded at around $700 \text{ cm}^2\text{V}^{-1}\text{s}^{-1}$ at room temperature, which is comparable with other 2D materials. In addition to these electrical devices, Te flakes have been used in optoelectrical device such as photodetectors [54] [55]. Recently, quantum effects have also been demonstrated using Te flakes. In Ref. [23], magneto-transport measurements were performed, and weak anti-localization (WAL) and universal conductance fluctuation (UCF) were observed at a low temperature (0.4 K). From the result of the temperature dependence of UCF, the group concluded that the c-axis electron transport was one dimensional when a magnetic field was applied along the c-axis. Other examples of observed quantum effects are the quantum Hall effect (QHE) and Shubnikov–de Haas (SdH) oscillation. Qiu et al. [56] succeeded in observing these two phenomena using a Te flake 10 nm in height. Since several quantum effects have been observed with Te flakes, a nanowire of Te may exhibit interesting electrical properties related to quantum effects. In this chapter, we investigated the electrical properties of the Te nanowires fabricated by physical vapor deposition in chapter 3.

4.2 Device fabrication

Te wires were grown by physical vapor deposition. Then, these wires were transferred using adhesive plastic film tape (ULTRON SYSTEMS, 1009R-6.0) onto a silicon substrate with 300 nm of thermal oxide as described in §3.3.1. Prior to fabricating the contacts on each wire,

the gold markers with height of 60 nm were fabricated in order to determine the position of each wire and make contact design on it. The process for fabricating the gold markers and contacts was summarized in Figure 4.1, and details of the fabrication recipe are described in Appendix. A dose of $180 \mu\text{C}/\text{cm}^2$ for electron beam lithography was chosen from the dose test results shown in Figure 4.2. During the device fabrication, the Te wires were exposed to the air, so their surfaces underwent oxidation. To remove the oxidized layer, device chips were immersed in 25 % hydrochloric acid (HCl) for 2 minutes. Gold was chosen for the metal contacts because its work function is compatible with that of tellurium. Tellurium is a p-type semiconductor, and its work function is 4.95 eV. Since the work function of gold is 5.10–5.47 eV, an Ohmic contact is formed between these materials. Because gold does not stick to SiO_2 substrate surface very well, 0.9 nm of chromium was used as an adhesion layer for the gold contacts. When the amount of evaporated chromium is large, a chromium film is deposited on the silicon substrate. If this evaporated quantity is reduced to a very small amount, chromium deposits in dots instead of a film. Although the work function of chromium is smaller than tellurium, Ohmic contact between gold and tellurium can be formed because Cr forms dots instead of a thin film. Also, the Cr thickness is less than a Fermi wavelength, which results in the Ohmic contact. The fabricated devices are shown in Figure 4.3. Degenerately doped Si substrates were used as back gates.

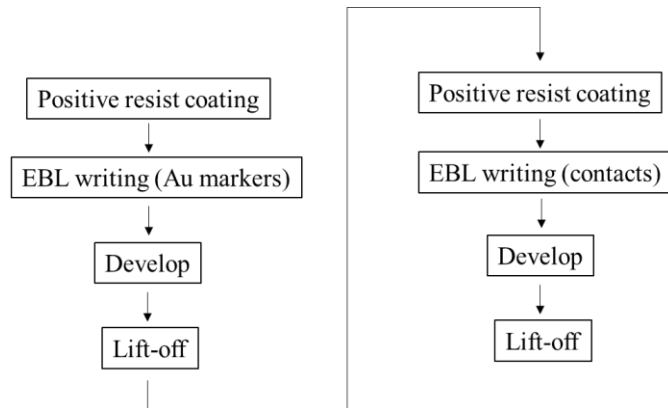


Figure 4.1: Contact fabrication process.

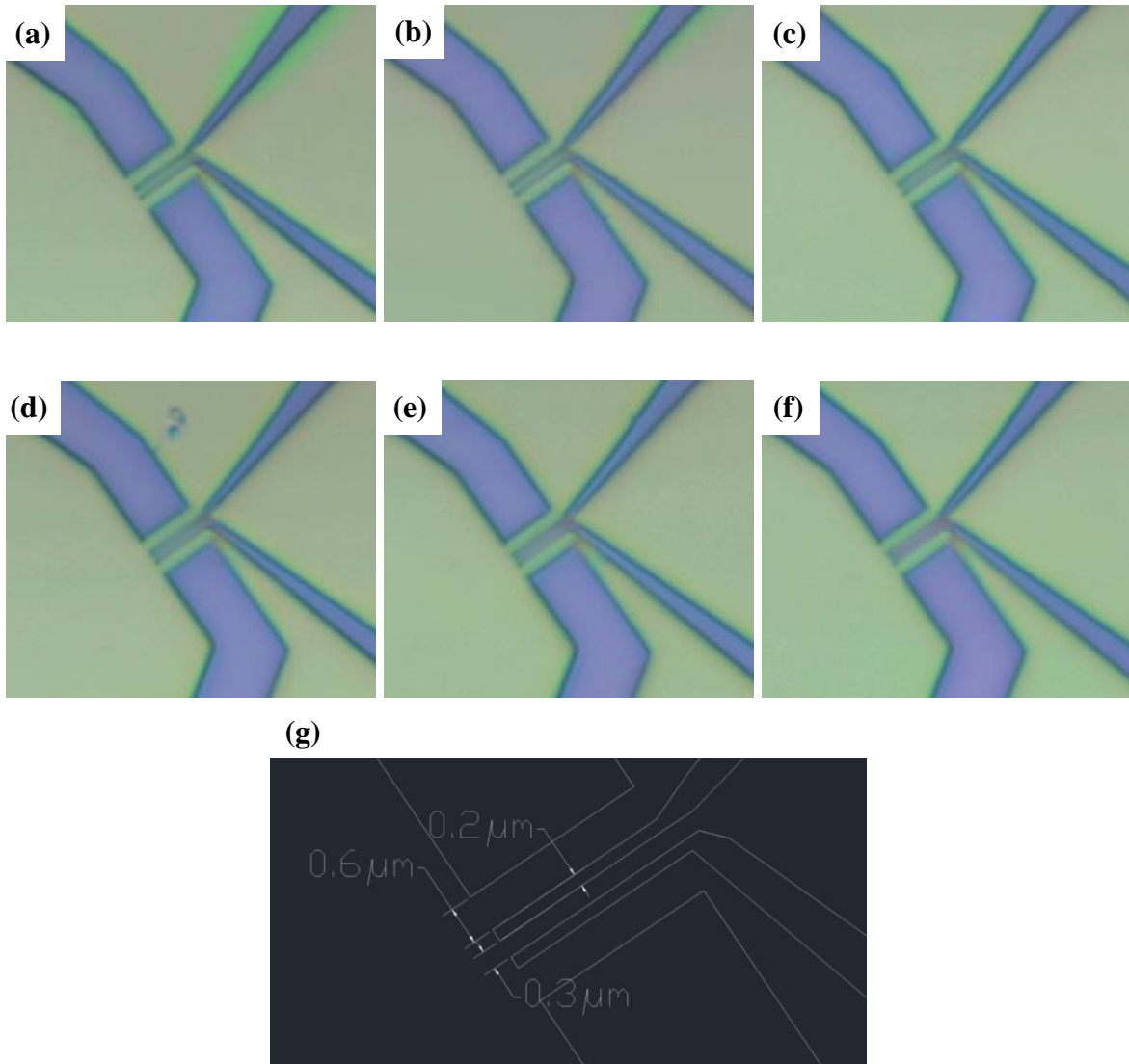


Figure 4.2: Optical microscopy images after the develop for dose test (a) 180 (b) 200 (c) 220 (d) 240 (e) 260 $\mu\text{C}/\text{cm}^2$. (g) Pattern design for the dose test.

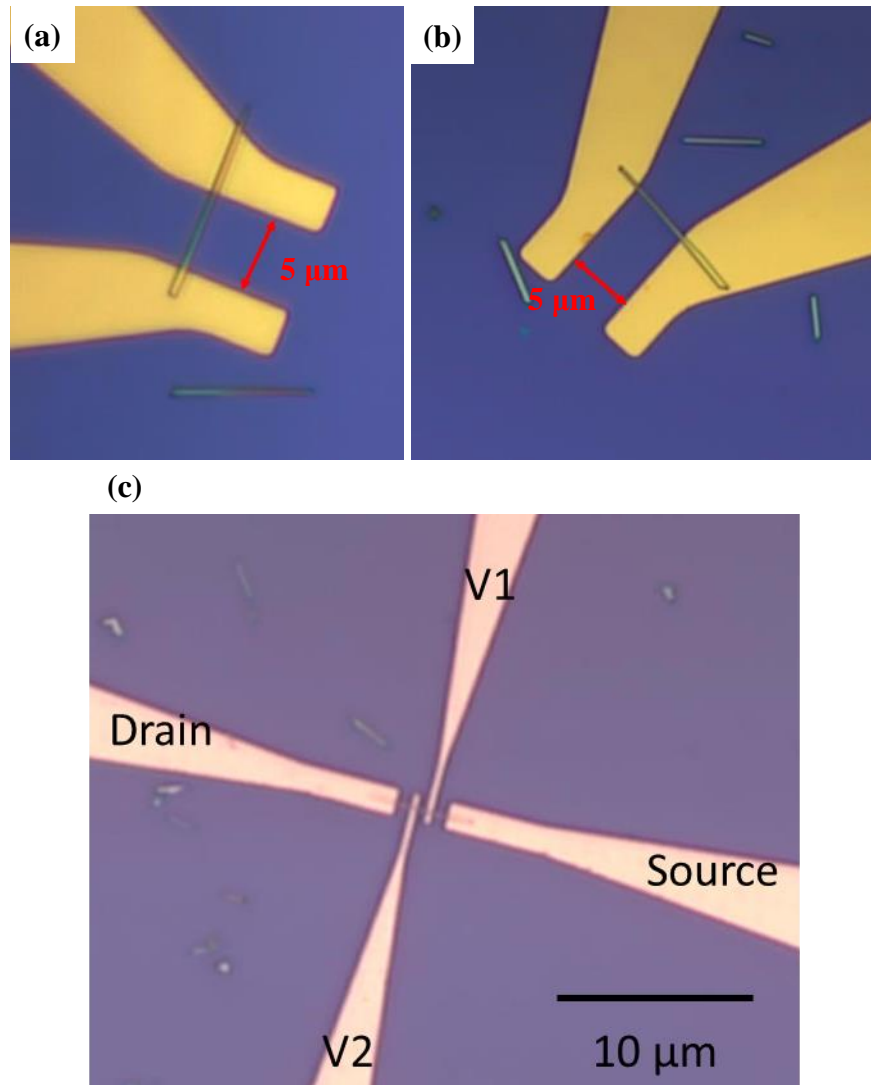


Figure 4.3: Optical microscopy images of Te wire Devices (a) 1-JA (b) 1-WI (c) 2-SF.

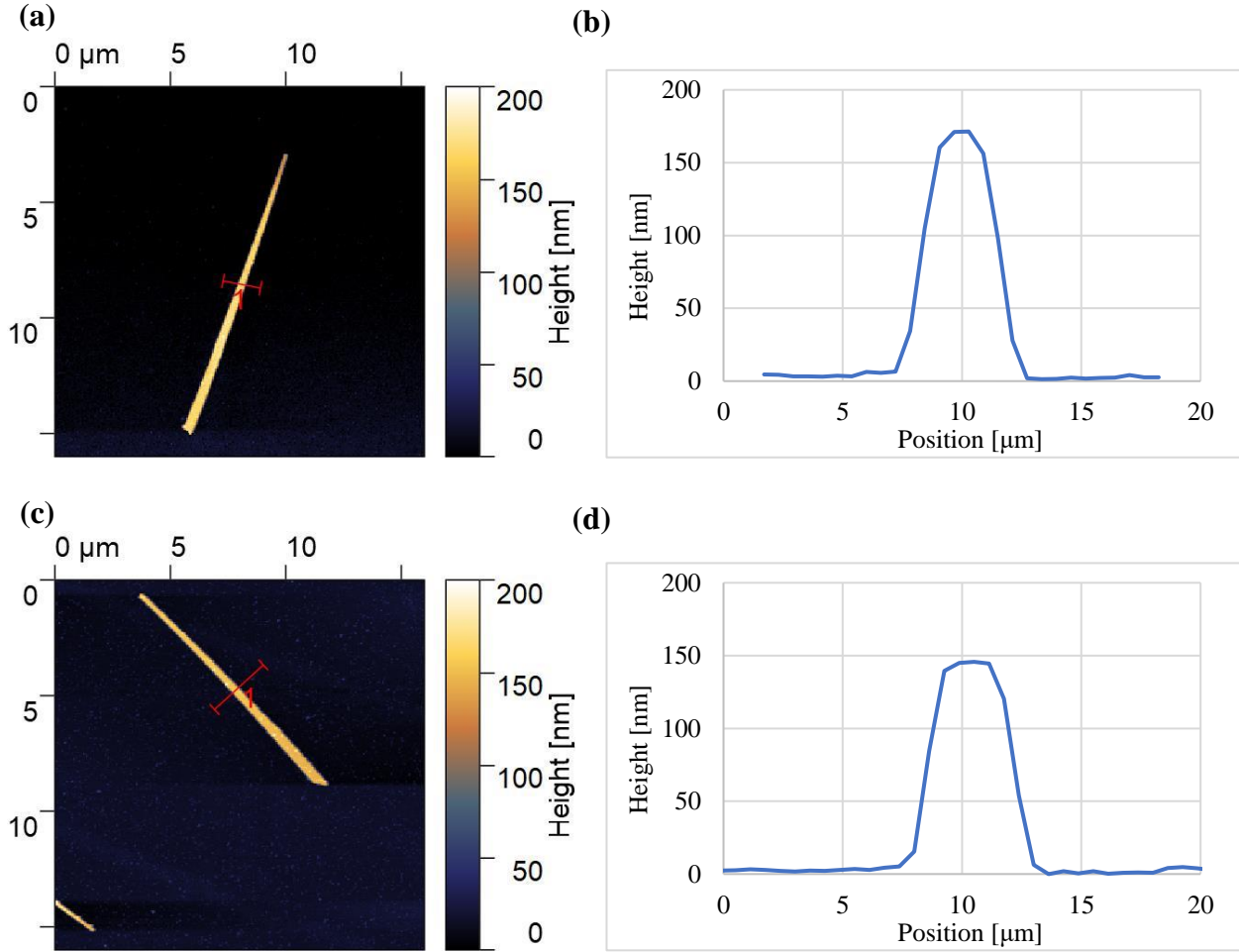


Figure 4.4: AFM image and height profile of Te wire for (a,b) device 1-JA and (c,d) device 1-WI.

4.3 Measurement set-ups

Transport measurements were performed using an optical cryostat (Figure 4.5 (a)). Because devices 1-JA and 1-MI had only 2 contacts, they were characterized by 2-wire resistance measurement. Regarding device 2-SF, a 4-wire resistance measurement was applied to measure the sample resistance more accurately. To measure the differential conductance, 2-wire voltage bias measurement was performed for each contact segment of device 2-SF using a lock-in amplifier technique. There are two methods to determine conductance: by calculation of $\frac{dI}{dV}$ from the I-V curve and by electrical method. For the former method, the I-V curve needs to be

analyzed after each measurement and a relatively large number of data points are required so that the differentiated graph is a smooth curve with low noise. For the latter method, low amplitude AC voltage is applied to the DC voltage as illustrated in Figure 4.7. This small voltage amplitude change induces a small AC current in the sample. By dividing measured AC current by applied AC voltage, we can obtain conductance directly during the I-V measurement. In our experiment, the sampling frequency of the lock-in amplifier was set to 73 Hz, and the output amplitude was set to either 150 or 32 mV to apply 150 μ V to Te wires (Figure 4.6).

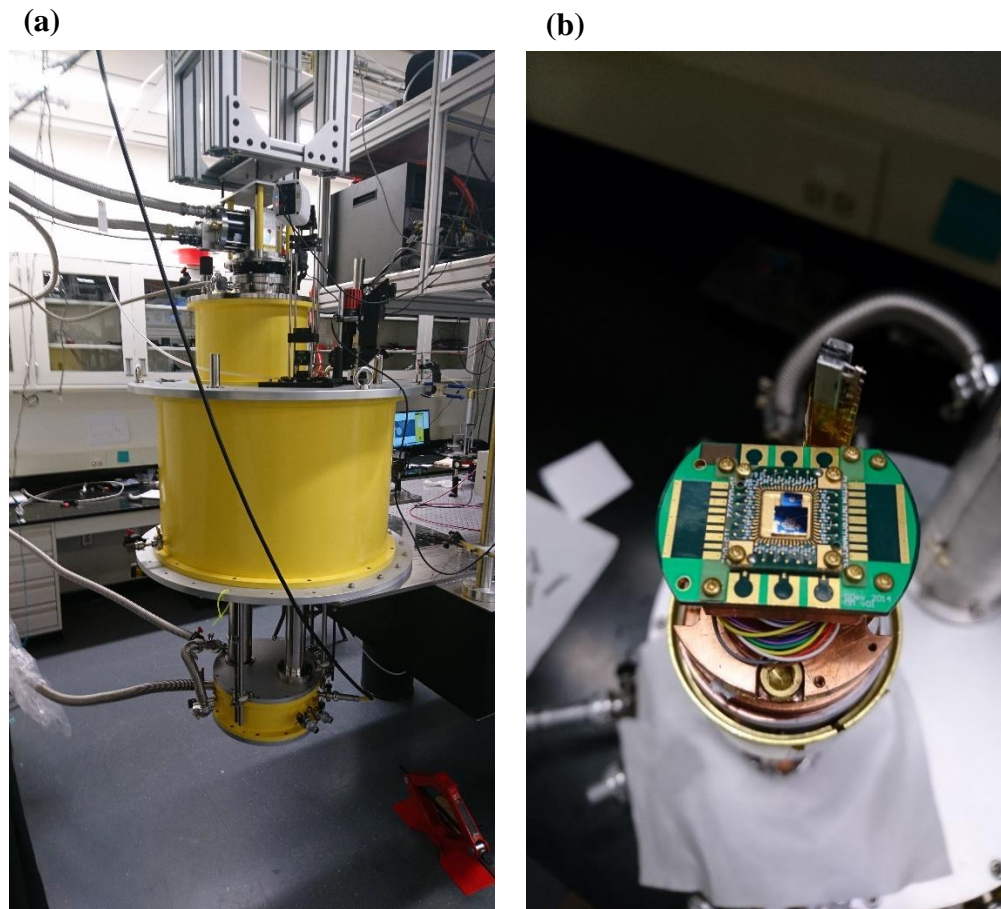


Figure 4.5: Image of (a) optical cryostat and (b) device.

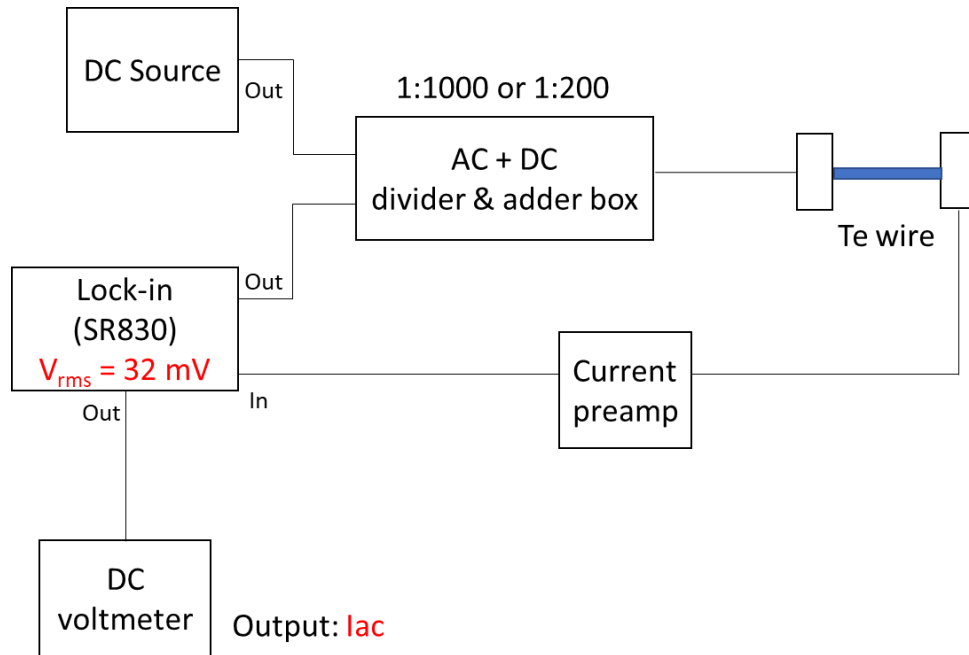


Figure 4.6: Schematic illustration of 2-wire voltage bias measurement.

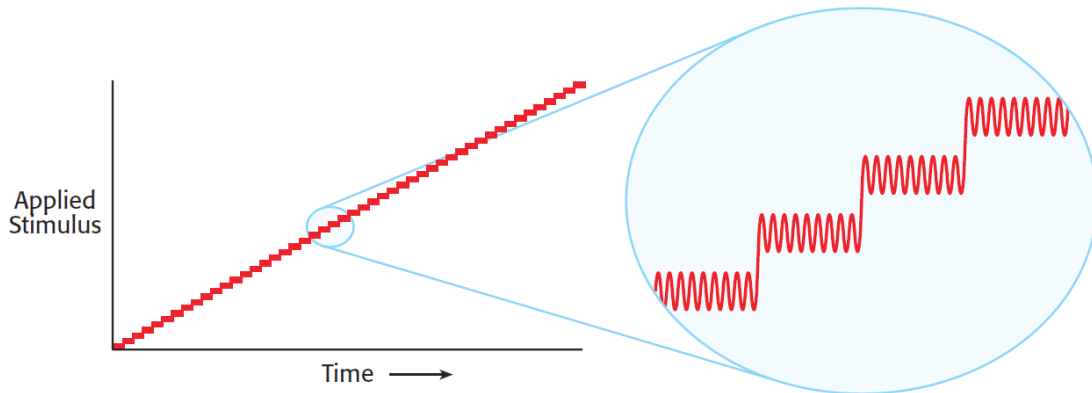


Figure 4.7: Schematic illustration of differential conductance by using DC + AC mixed source signal [57].

4.4 I-V curve

Figure 4.8 and Figure 4.9 indicate the I-V curve results for each device at room temperature and low temperature. All measurements were conducted at $V_g=0\text{ V}$. At room temperature, all devices showed a linear relationship between the bias voltage (V_{sd}) and the drain current (I_{sd}), which indicates that Ohmic contacts were formed between the Te wires and

the gold contacts. At low temperature, device 1-JA exhibited a linear I-V curve, but device 1-WI and 2-SF exhibited non-linear I-V curves. These non-linear curves can be attributed to the Schottky barrier. At room temperature, the thermal energy is high enough to overcome this barrier, but at low temperature, thermionic emissions were likely restricted due to this small barrier. There are several possible reasons a non-linear I-V curve was produced such as impurities and an oxidation layer on Te surface, but devices 1-JA and 1-WI were fabricated using the same procedure, and they were on the same substrate. Generally, there were several devices on a substrate so that the transport measurement could be conducted on multiple samples in succession. Although the fabrication process was the same for all devices on the substrate, only a few devices worked each time. This seems to suggest that the quality of the Te wire may be a contributing factor to a non-linear I-V curve result.

Finally, Figure 4.10 shows the temperature dependence of I_{sd} versus the back gate voltage (V_g) for devices 1-JA and 2-SF. For (a) and (d), there are two lines for each temperature curve. This is the hysteresis due to the charge accumulation during gate voltage sweeping. The resistance of device 1-JA decreased with decreasing temperature due to the decrease of electron scattering, which indicates that this Te wire is made of high quality Te crystal. On the other hand, device 2-SF showed decreasing resistance until around 240 K, but it exhibited an increase of the resistance below 240 K that can be attributed to the fact that the Schottky barrier is dominant below 240 K.

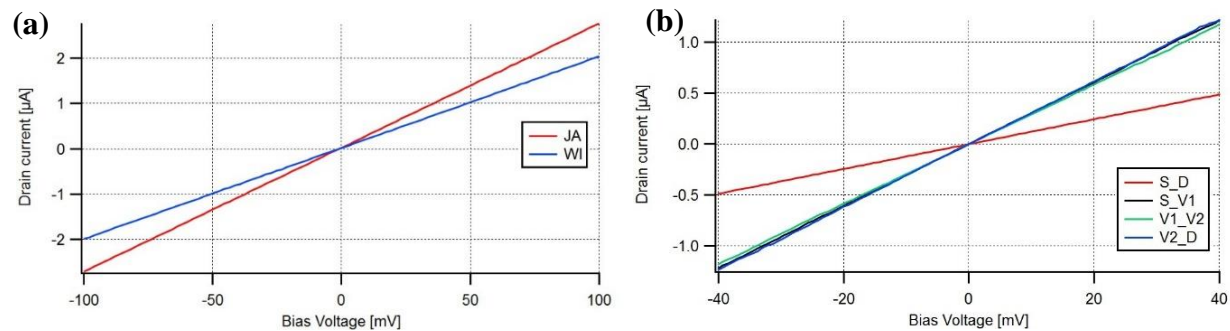


Figure 4.8: I-V curve at room temperature: (a) device1-JA and 1-WI (b) device 2-SF.

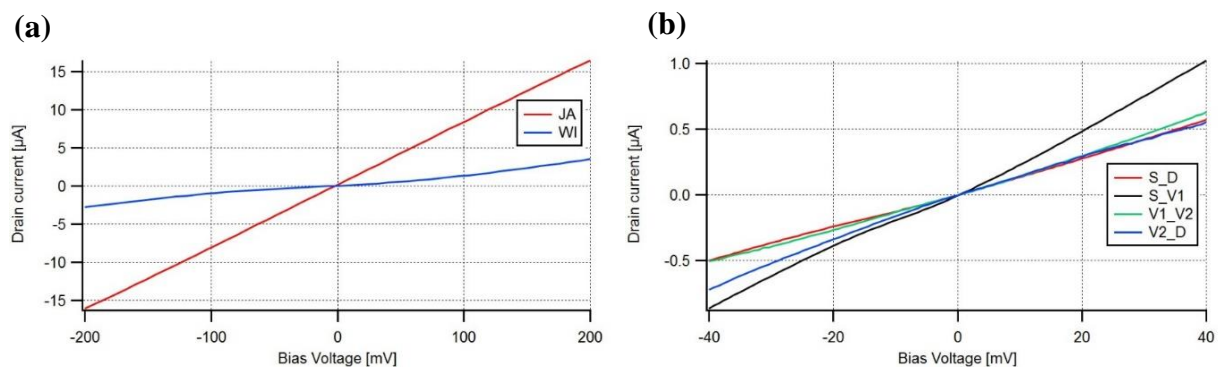


Figure 4.9: I-V curve at low temperature: (a) device1-JA and 1-WI at 10 K. (b) device 2-SF at 2.8 K.

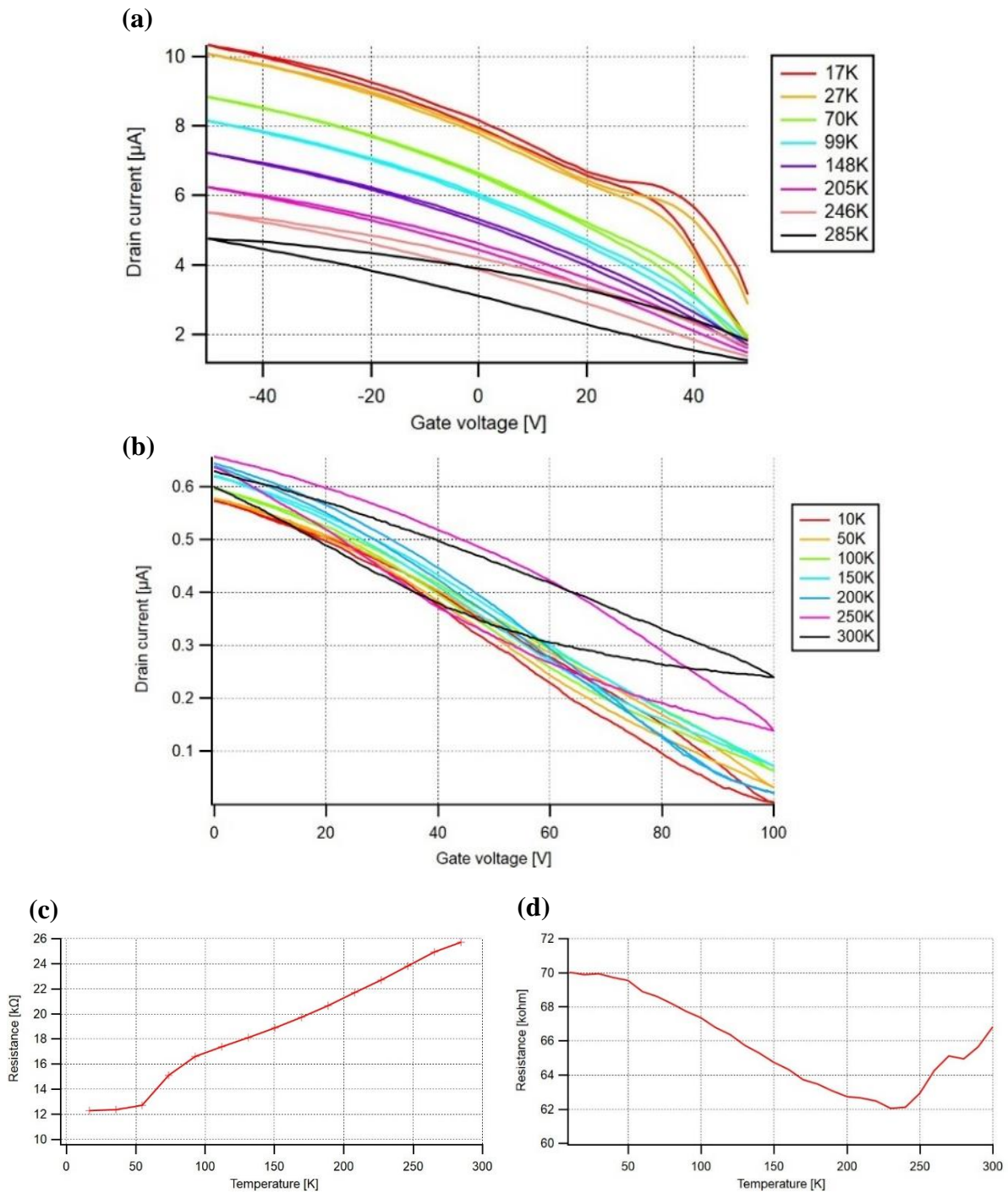


Figure 4.10: Temperature dependence of I_{sd} versus V_g for (a) device 1-JA and (b) device 2-SF, and temperature dependence of resistance of for (c) device 1-JA and (d) device 2-SF. (c) and (d) were calculated from I_{sd} and V_{sd} at $V_g=0$ V.

4.5 Contact resistance and resistivity of device 2-SF

From the low temperature I-V curve of device 2-SF (Figure 4.9), we estimated its contact resistance. Figure 4.11 is the schematic illustration of the 4-terminal contact. The assumption is made that each contact had the same resistance and that the resistivity of the Te wire was homogeneous. From the intrinsic Te wire resistance $R_{XX} = \frac{V_{XX}}{I_{sd}}$ and the 2-terminal resistance $R_{2T} = \frac{V_{sd}}{I_{sd}}$, the contact resistance R_C was calculated by the following equation.

$$R_C = \frac{R_{2T} - R_{XX} \frac{L_{2T}}{L_{XX}}}{2} \quad (4.1)$$

Table 4.1 and Table 4.2 show the structure size of device 2-SF and the measured current and voltage. The device structure size is the assumed value since the device was damaged and could not be measured. By substituting these values, the contact resistance was calculated as -13 k Ω . Equation (4.1) assumes that the resistivity of the Te wire is homogeneous along the wire direction. Since a negative contact resistance was calculated, this assumption was not valid for this experimental result.

Table 4.1: Device structure size (Original design value)

Contact geometry size (Original design value)	Width of inner electrodes Δ [nm]	300
	Inner electrode distance L_{2T} [nm]	500
	Outer electrode distance L_{XX} [nm]	2700
Te wire size	Height [nm]	70
	Width [nm]	300

Table 4.2: Four-terminal measurement result

Temperature [K]	2.8	300
Drain current I_{sd} [nA]	571	489
Bias voltage V_{sd} [mV]	40	40
Voltage drop between inner electrodes V_{XX} [mV]	10.26	12.32
Intrinsic Te wire resistance R_{XX} [k Ω]	18	25
Two-terminal resistance R_{2T} [k Ω]	70	82

The non-linear resistivity can be attributed to two possible causes. The first of these is the low quality or deficiency of the Te wire, which may have contributed to additional resistance in the region between the inner two electrodes. The second is non-uniform current density distribution due to the metal contact and sample geometry [58]. In this case, a correction factor F needs to be added to the material resistivity. In Ref. [58], the correction factor was simulated by using a finite element model, and it was simulated using three parameters: electrode ratio ER , effective thickness ratio TR_{eff} , and interface resistance factor α . The electrode ratio ER is expressed as $ER = \frac{\Delta}{s}$, where Δ is the width of an electrode and s is the electrode distance, and it is calculated to be $ER = \frac{300 \text{ nm}}{500 \text{ nm}} = 0.6$. However, we assumed $ER = \frac{400 \text{ nm}}{400 \text{ nm}} = 1$ since the actual device size is unknown, and since the electrode width may have increased after the electron beam lithography. The effective thickness ratio is expressed as $TR_{eff} = \frac{t\sqrt{\xi}}{s}$, where t is the thickness of the sample and ξ is the in-plane and transverse resistivity ratio ($\xi = \frac{\rho_z}{\rho_x}$). According to Ref. [26], the field-effect mobility ratio of the c-axis and a-axis was estimated as $\frac{\mu_{c-axis}}{\mu_{a-axis}} = 1.43$. From this result, the in-plane and transverse resistivity ratio ξ is assumed to be $\xi = \frac{\rho_{a-axis}}{\rho_{c-axis}} = 1.43$. Thus, the effective thickness ratio TR_{eff} was obtained as $TR_{eff} = \frac{70\sqrt{1.43}}{400} = 0.2$. The interface resistance factor is expressed as $\alpha = \frac{R_c}{R_{XX}}$. At first, we assumed $\alpha \gg 1$ since the resistance increased with decreasing temperature (Figure 4.10 (d)). In this case the correction factor $F = 0.5$ was obtained [58], and the contact resistance was calculated as 6 k Ω at 2.8 K by using the following equation .

$$R_c = \frac{R_{2T} - F(R_{XX} \frac{L_{2T}}{L_{XX}})}{2} \quad (4.2)$$

In this case, the interface resistance factor would be $\alpha = \frac{R_c}{R_{XX}} = \frac{6}{25} < 1$, which is inconsistent with the assumption of $\alpha \gg 1$. Thus, we assumed $\alpha = 0.1$ and obtained the correction factor $F = 0.6$ from Figure 4.12 (b). Also, when $\alpha = 0.1$, the current flows inside the gold contact as illustrated in Figure 4.13 because the contact resistance is lower than the Te wire resistance. In this case, the Te wire length in which the current flows is shortened by the width of the two inner electrodes. From this assumption and the correction factor $F=0.6$, we calculated the contact resistance and resistivity of the Te wire. The resistivity of the Te wire was calculated by Equation (4.3), where w is the width of the Te wire. Table 4.3 shows the assumed device structure size and Table 4.4 shows the calculated result.

$$\rho = R_{XX} \frac{wt}{L_{XX}} \quad (4.3)$$

Table 4.3: Assumed device structure size

Contact geometry size (Original design value)	Width of inner electrodes Δ [nm]	400
	Inner electrode distance L_{2T} [nm]	400
	Outer electrode distance L_{XX} [nm]	1900
Te wire size	Height t [nm]	70
	Width w [nm]	300

Table 4.4: Calculated contact resistance and resistivity by using the correction factor $F=0.6$

	Temperature [K]	
	2.8	300
Contact resistance R_C [k Ω]	9.4	5
Resistivity ρ [$\Omega \cdot m$]	9.4×10^{-4}	1.3×10^{-3}

The resistivity of bulk Te along the c-axis at room temperature is $2.6 \times 10^{-3} \Omega \cdot m$ [16]. At room temperature, the calculated resistivity was $1.3 \times 10^{-3} \Omega \cdot m$, which is in the same order of magnitude as the bulk resistivity value. Table 4.4 indicates that the contact resistance

increased while the resistivity decreased with decreasing temperature, which seems to be a reasonable interpretation from the results of the temperature dependence of resistance (Figure 4.10 (d)) expected as the probability of thermal excitation over the Schottky barrier decreases exponentially with decreasing temperature. Since the actual size of the device is unknown, this result is more likely qualitative.

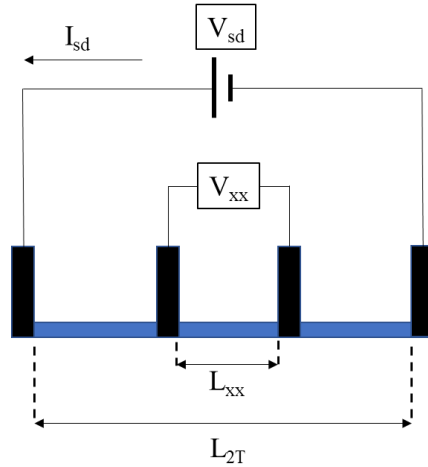


Figure 4.11: Schematic illustration of 4-wire resistance measurement.

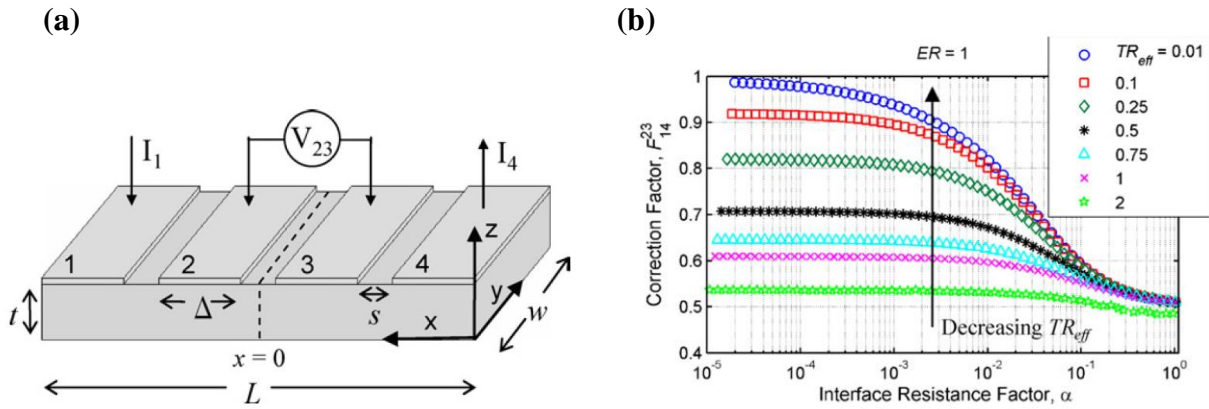


Figure 4.12: (a) Schematic illustration of contact and sample geometry and (b) simulation result of correction factor in Ref. [58].

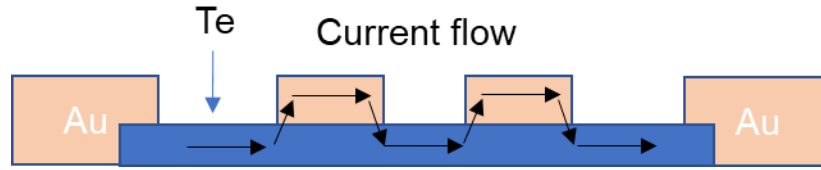


Figure 4.13: Schematic illustration of the current flow when the contact resistance is lower than the intrinsic Te wire resistance.

4.6 Conductance

To characterize Device1-JA and 1-WI, the source-drain current was measured at each gate voltage. Figure 4.14 shows the drain current as a function of bias and gate voltages for devices 1-JA and 1-WI at 10 K. The transconductance of both devices was obtained by taking the derivative of $\frac{dI_{sd}}{dV_g}$ from Figure 4.14 (a) and (b). Regarding Figure 4.14 (c), there are two extreme values at both the negative and positive bias voltages, which indicates that the current increase (the slope of the I_{sd} and V_g curve) was hindered between the gate voltage of 40–20 V. This could be due to interband scattering [59]. The gate voltage controls the Fermi energy of the Te wire. Since Te is a p-type semiconductor, the Fermi energy at $V_g > 60$ V is located above the highest valence band (Figure 4.15 (a)). Decreasing the gate voltage caused the Fermi energy to overlap the highest valence band (Figure 4.15 (b)). However, when $V_g = 40$ V, the Fermi energy reached another band (Figure 4.15 (c)), which enabled holes from both bands to contribute to the current flow. This interband transition created hole scattering, causing the current to decrease.

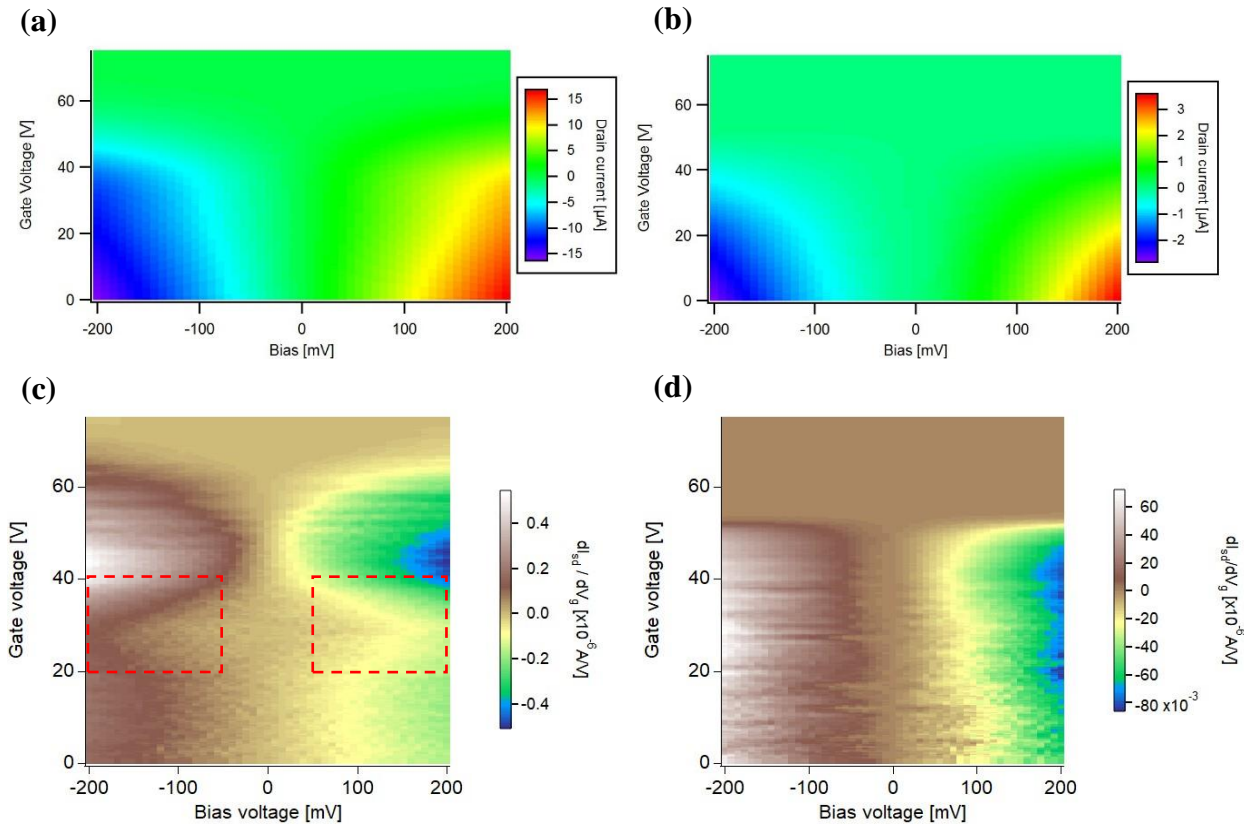


Figure 4.14: Drain current map of device (a) 1-JA and (b) 1-WI. Transconductance map of device (c) 1-JA and (d) 1-WI. The dashed red areas in (c) indicate the current decrease due to the interband scattering.

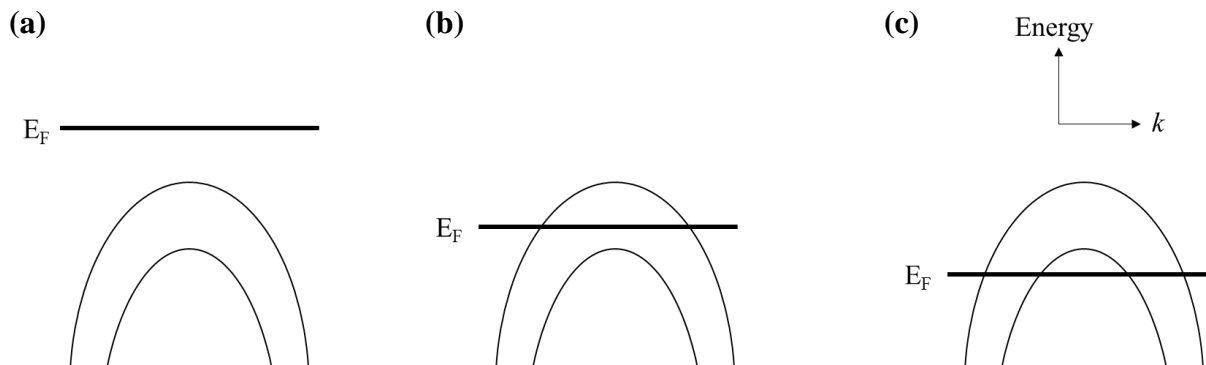


Figure 4.15: Schematic illustration of the relationship between the Fermi energy and valence subbands (a) $V_g > 60$ V (b) 40 V $< V_g < 60$ V (c) 20 V $< V_g < 40$ V for device 1-JA.

Figure 4.16 shows the conductance map of device 2-SF for each contact segment by using the differential conductance technique described in §4.3. The measured conductance is

represented in the unit of quantum conductance $\frac{e^2}{h}$ (3.874×10^{-5} S), where e is the charge of an electron and h is the Plank constant. The source voltage was applied in the order of each segment name. For example, the current flows from S to V1 in the case of the S-V1 segment. At the S-D and S-V1 regions, the conductance is asymmetric regarding the positive and negative V_{sd} , which indicates that the conductance (the slope of I-V curve) is increasing with bias voltage. Another remarkable point is that there are diamond shaped patterns (conductance plateaus) at $V_g = 40\text{--}60$ V in the V1-V2 and V2-D regions. This type of pattern appeared in ballistic electron transport [60] and quantum point contacts [61]. However, the patterns in Figure 4.16 (c) and (d) can be attributed to the V2 contact interface because this pattern does not appear in the S-D and S-V1 regions and because the pattern is symmetric when the bias voltage is applied in the opposite direction (V1-V2 and V2-D). Generally, the value of conductance is in the order of $\frac{e^2}{h}$ quantum transport. Our measurement showed that the conductance was lower than $\frac{e^2}{h}$, indicating that the electron transport was not ballistic. Although the diamond shaped pattern is not a feature of ballistic transport, we focused on the V2-D region to investigate this pattern further.

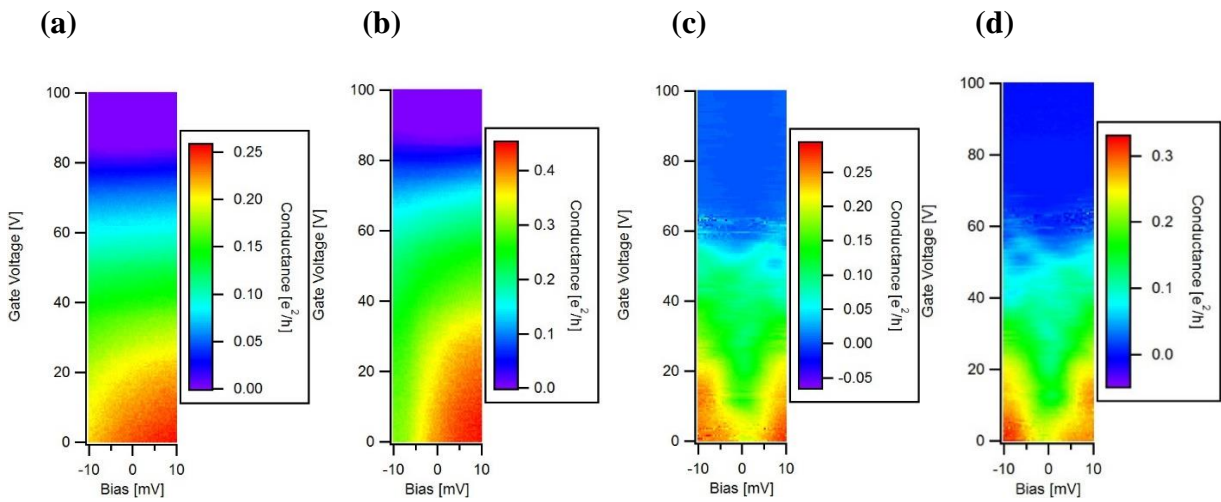


Figure 4.16: Conductance map of device 2-SF for each segment: (a) S-D (b) S-V1 (c) V1-V2 (d) V2-D.

4.7 Magnetic field dependence of device 2-SF conductance

We applied up to 8 tesla to device 2-SF. Figure 4.17 shows the conductance map with and without a magnetic field perpendicular to the device substrate at low temperature. By increasing the bias range, the diamond shaped structure is clearly seen in this figure, but there is no significant difference in structure between (a) and (b). To observe the small differences between (a) and (b), we measured the magnetic field dependence of the conductance at 0 bias voltage (Figure 4.18 (a)). Figure 4.18 (b) is the extracted data from (a) at $B=2$ T. From this figure, it is obvious that the conductance decreases by steps with increasing the gate voltage. From Figure 4.18 (a), the position of the conductance plateau at around $V_g = 57$ V slightly shifted from lower to higher gate voltages with decreasing the magnetic field. This shift is indicated as a dashed red line.

The reason for obtaining the conductance plateaus is not clear, but we estimated g-factor from the following equation [60].

$$E = g\mu_B B \quad (4.4)$$

where E is the energy, and μ_B is the Bohr magneton ($\mu_B = 5.788 \times 10^{-5} \text{ eVT}^{-1}$), and B is the magnetic field. To obtain energy E , the lever arm α (the unit of α is eVV^{-1}) needs to be calculated from the conductance plateaus. The lever arm α is calculated from the following equation as illustrated in Figure 4.19.

$$\alpha = \frac{\Delta E_{\text{subband}}}{\Delta V_G} = \frac{\Delta V_{SD}}{\Delta V_G} \quad (4.5)$$

Figure 4.17 (c) is the extracted data from Figure 4.17 (a). By focusing the uppermost conductance plateau in this figure, the lever arm α was calculated as $\alpha = \frac{5.2 \times 10^{-3}}{10} = 0.52 \text{ meVV}^{-1}$.

The slope of the conductance plateau indicated in Figure 4.18 (a) by the dashed red line was obtained by the conductance curve fitting expressed as the following equation.

$$G(x) = A + B \tanh(-x + C)$$

where A , B and C are coefficient values. Since the coefficient C is the middle point of two conductance plateaus, we considered this point to be a conductance plateau edge. Figure 4.18 (c) indicates a fitting result for the conductance curve at $B=2$ T, and coefficient C was obtained as 57.354 V. Figure 4.18 (d) shows coefficient C obtained by curve fitting as a function of magnetic field. From the linear fit of Figure 4.18 (d), the slope of the conductance plateau change was determined to be 0.043 VT^{-1} , and the gate voltage shift of the conductance plateau edge was calculated as $0.043 \text{ VT}^{-1} \times 8 \text{ T} = 0.34 \text{ V}$. From this value, the energy E was calculated as $\alpha \times 0.34 = 0.18 \text{ meV}$. By substituting $E=0.18 \text{ meV}$, $\mu_B = 5.788 \times 10^{-5} \text{ eVT}^{-1}$, and $B=8 \text{ T}$ into Equation (4.6), the g-factor was calculated to be 0.39. The g-factor of an electron in a vacuum and of bulk tellurium with a magnetic field parallel to the c-axis are 2 and 5 [62], respectively. It is known that the g-factor is dependent on the direction of the magnetic field [63]. Thus, the relatively low g-factor that was obtained might be due to the magnetic field direction.

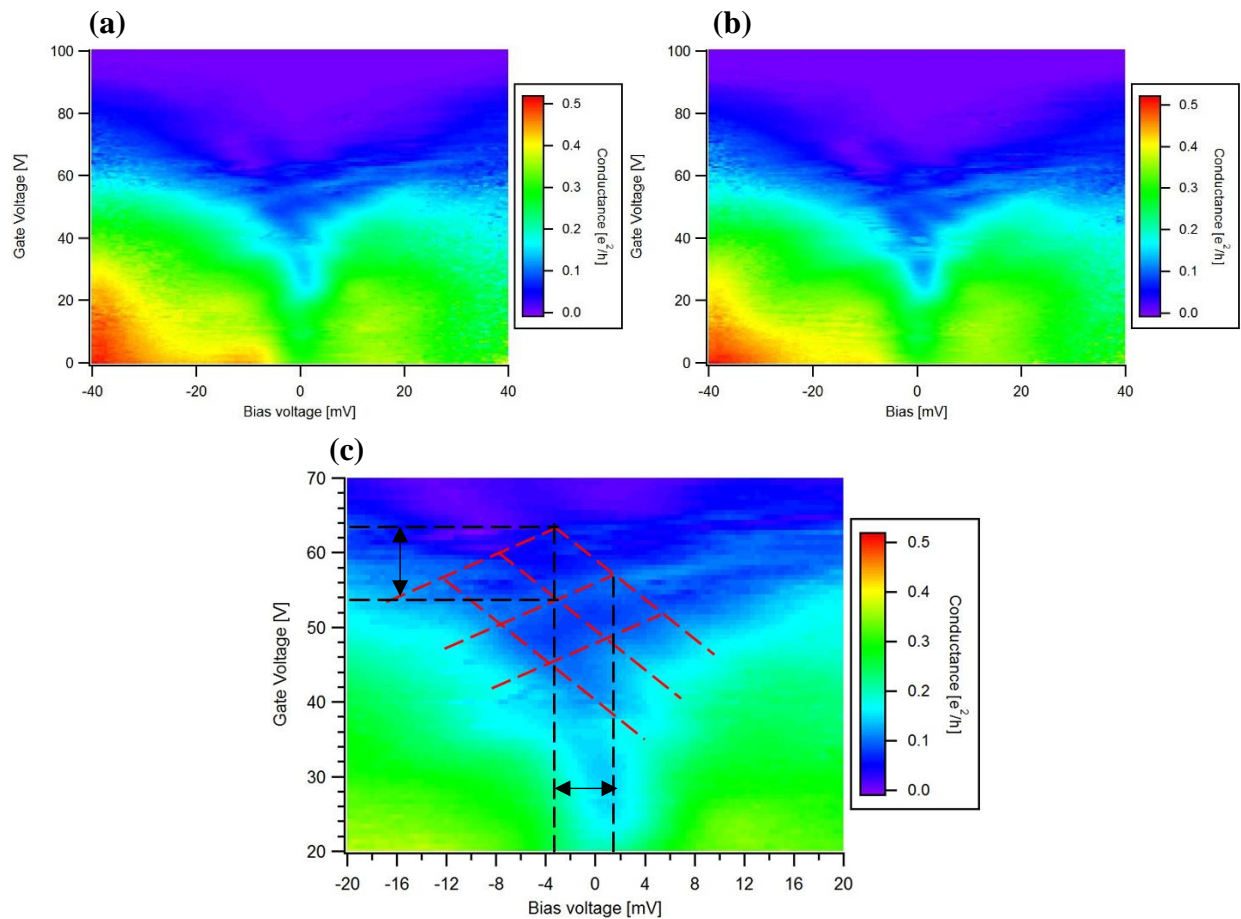


Figure 4.17: Conductance map with (a) 0 T (b) 8 T magnetic field (c) extracted data from (a). The dashed red lines in (c) are the guide lines to the eye, indicating the conductance plateaus.

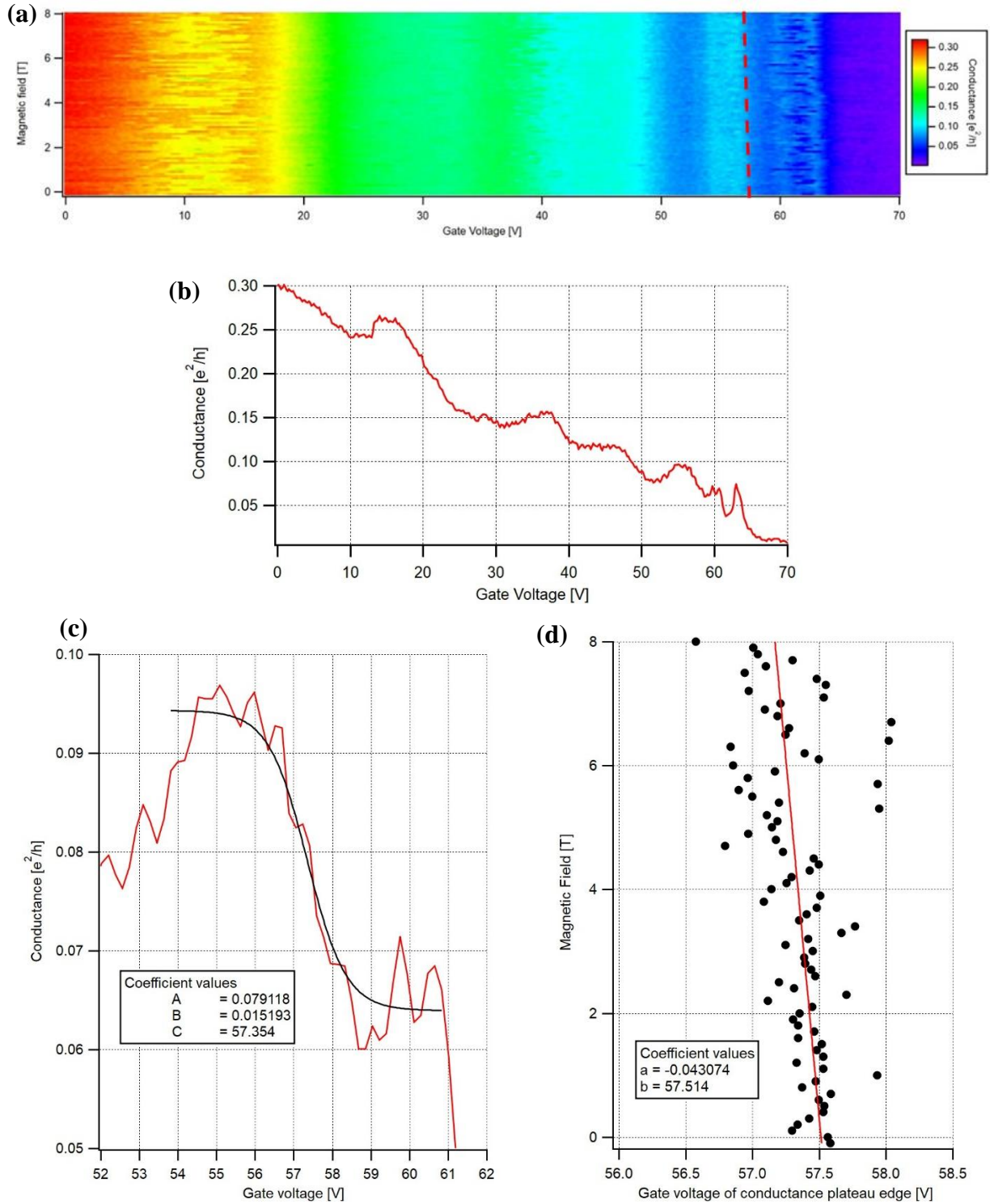


Figure 4.18: (a) Magnetic field dependence of quantized conductance at $V_{sd} = 0$ V. The dashed red line is a guide line for the eye, indicating the conductance plateau shift. (b) Extracted data at $B=2$ T from (a). (c) Conductance curve fitting for (b) at $V_g=54-61$ V. (d) The slope of the conductance plateau at around $V_g=57$ V. The gate voltage of the conductance plateau edge was obtained from the coefficient C of the fitting curve $G(x) = A + B \tanh(-x + C)$.

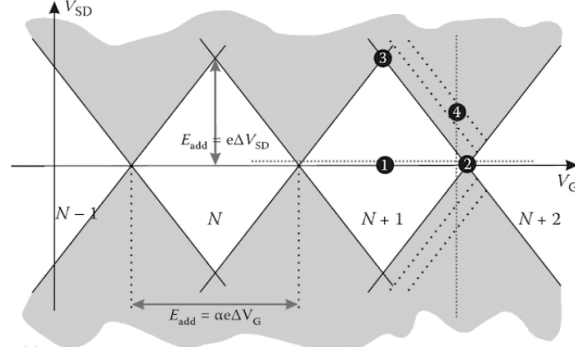


Figure 4.19: Calculation of lever arm α from conduction plateaus ($\alpha = \frac{\Delta V_{SD}}{\Delta V_G}$) [64].

4.8 Mobility

We estimated the mobility using the following equation [65],

$$\mu = \frac{g_m L_G^2}{C V_{sd}} \quad (4.7)$$

where $g_m = \frac{dI_{sd}}{dV_g}$, L_G is the gate length, C is the capacitance of the wire, and V_{sd} is the bias

voltage. Capacitance C was calculated by using Equation (4.8) [65],

$$C = \frac{2\pi\epsilon L_G}{\ln \left[\frac{t_{ox} + a + \sqrt{(t_{ox} + a)^2 - a^2}}{a} \right]} \quad (4.8)$$

where ϵ is the insulator dielectric constant, t_{ox} is the insulator thickness, and a is the Te wire radius. Table 4.5 lists the parameters used for estimating the mobility for device 1-JA and device 2-SF, and Table 4.6 shows the calculated mobility.

Table 4.5: Mobility calculation parameters

Device	1-JA		2-SF	
Temperature [K]	10	300	2.8	300
ϵ_0 [Fm ⁻¹]	8.9×10^{-12}			
ϵ	3.9			
L_g [μm]	5.0		2.7	
t_{ox} [nm]	300			
a [nm]	80		35	
C [F]	4.8×10^{-16}		3.7×10^{-17}	
V_{sd} [mV]	200	100	10	12.3
g_m [S]	4.0×10^{-7}	3.8×10^{-8}	7.5×10^{-9}	4.3×10^{-9}

Table 4.6: Mobility calculation result

Device	1-JA		2-SF	
Temperature [K]	10	300	2.8	300
Mobility [cm ² V ⁻¹ s ⁻¹]	1032	194	51	23

Device 2-SF showed much lower mobility than device 1-JA. This can be attributed to the low quality of the Te nanowire since the mobility of device 2-SF was measured by 4-terminal measurement. Regarding device 1-JA, it showed a mobility of 1032 cm²V⁻¹s⁻¹. In Ref. [53], a Te wire was fabricated on a SiO₂ substrate by molecular beam epitaxy (MBE), and a mobility of 707 cm²V⁻¹s⁻¹ was obtained at room temperature. Also, in Ref. [26], a Te flake with 15 nm thickness showed around 700 cm²V⁻¹s⁻¹ mobility at room temperature. In our experiment, device 1-JA showed a mobility of 194 cm²V⁻¹s⁻¹ at room temperature, which was much lower than that of these two references. One possible reason is the difference of the growth method. The Te wire grown by MBE [53] might be higher crystal quality than that of physical vapor deposition.

Chapter 5 Summary and future work

5.1 Summary

This research focused on the characterization of nanoscale Te obtained by exfoliation and physical vapor deposition. Mechanical exfoliation, that is manually rubbing a single Te crystal on SiO₂ substrates, was demonstrated to fabricate thin Te flakes with heights of 10–15 nm and ultra-thin wires with heights of 1–2 nm and lengths of around 100 nm. The chain direction of ultra-thin wires was determined by polarized Raman spectroscopy, and this technique was useful for samples whose chain direction was ambiguous from optical microscope images. However, the probability of producing thin flakes and wires by mechanical exfoliation was quite low, thus, we conclude that exfoliation is likely not a viable route for synthesizing single atom chains.

For the purpose of creating single atom chains, we investigated Te and Se crystal synthesis on SiO₂ substrates and r-plane sapphire substrates with atomic steps by physical vapor deposition. Single crystal wires were fabricated from the amorphous Te or Se seeds. By applying the standard tape exfoliation method to grown Te and Se crystals, Te flakes with a height of 60 nm and Se flakes with a height of 30–40 nm were obtained. There was no significant difference between SiO₂ and r-plane sapphire substrates with atomic steps.

Transport measurements were carried out on three Te nanowire devices: 1-JA (2-terminal), 1-WI (2-terminal), and 2-SF (4-terminal). Devices 1-JA and 2-SF exhibited a field effect mobility of 1032 cm²V⁻¹s⁻¹ and 51 cm²V⁻¹s⁻¹, respectively, at low temperature. The difference in these mobilities can be attributed to the quality of the nanowire. From the 4-terminal measurement of device 2-SF, the contact resistance and resistivity of Te were estimated to be 9.4 kΩ and 9.4×10⁻⁴ Ω · m at a temperature of 2.8 K by applying a correction factor of 0.6 to correct for the non-uniform current density distribution inside the nanowire.

5.2 Future work

We were not able to synthesize Te or Se single atom chains using atomic step substrates with physical vapor deposition. However, it would be quite interesting to apply molecular beam epitaxy (MBE) to an atomic step substrate since ultra-thin MoS₂ wires with three atomic chains were demonstrated by combining MBE and an atomic step gold substrate [45]. Several studies succeeded in the synthesis of a few layers of Te by MBE on both a graphene/6H-SiC(0001) substrate [21] and a highly oriented pyrolytic graphite (HOPG) substrate [66]. One of the issues with MBE growth is lattice matching between the target material and the substrate, though this has been overcome by applying van der Waals (vdW) epitaxy in Ref. [21]. To our knowledge, MBE growth of selenium has not been reported by any groups. Selecting the proper substrate with atomic steps could be an issue for the growth of Te and Se single atom chains, but this method is thought to be a promising route for their synthesis.

Meanwhile, further investigation about transport measurement of Te nanowires is essential since Te has the potential of exhibiting quantum effects due to its high mobility and strong spin-orbit interaction. For instance, simply changing the insulator from SiO₂ to higher quality ones such as hafnium oxide and hexagonal boron nitride and by decreasing the gate length, ballistic transport could be observed.

References

- [1] Y. Cui, Q. Q. Wei, H. K. Park, and C. M. Lieber, "Nanowire nanosensors for highly sensitive and selective detection of biological and chemical species," *Science*, vol. 293, no. 5533, pp. 1289-1292, Aug 2001.
- [2] Q. Wan *et al.*, "Fabrication and ethanol sensing characteristics of ZnO nanowire gas sensors," *Applied Physics Letters*, vol. 84, no. 18, pp. 3654-3656, May 2004.
- [3] G. F. Zheng, F. Patolsky, Y. Cui, W. U. Wang, and C. M. Lieber, "Multiplexed electrical detection of cancer markers with nanowire sensor arrays," *Nature Biotechnology*, vol. 23, no. 10, pp. 1294-1301, Oct 2005.
- [4] X. F. Duan, Y. Huang, R. Agarwal, and C. M. Lieber, "Single-nanowire electrically driven lasers," *Nature*, vol. 421, no. 6920, pp. 241-245, Jan 2003.
- [5] M. H. Huang *et al.*, "Room-temperature ultraviolet nanowire nanolasers," *Science*, vol. 292, no. 5523, pp. 1897-1899, Jun 2001.
- [6] P. D. Yang *et al.*, "Controlled growth of ZnO nanowires and their optical properties," *Advanced Functional Materials*, vol. 12, no. 5, pp. 323-331, May 2002.
- [7] H. Kind, H. Q. Yan, B. Messer, M. Law, and P. D. Yang, "Nanowire ultraviolet photodetectors and optical switches," *Advanced Materials*, vol. 14, no. 2, pp. 158+, Jan 2002.
- [8] C. Soci *et al.*, "ZnO nanowire UV photodetectors with high internal gain," *Nano Letters*, vol. 7, no. 4, pp. 1003-1009, Apr 2007.
- [9] Y. Cui and C. M. Lieber, "Functional nanoscale electronic devices assembled using silicon nanowire building blocks," *Science*, vol. 291, no. 5505, pp. 851-853, Feb 2001.
- [10] Y. Cui, Z. H. Zhong, D. L. Wang, W. U. Wang, and C. M. Lieber, "High performance silicon nanowire field effect transistors," *Nano Letters*, vol. 3, no. 2, pp. 149-152, Feb 2003.
- [11] Y. Huang, X. F. Duan, Y. Cui, L. J. Lauhon, K. H. Kim, and C. M. Lieber, "Logic gates and computation from assembled nanowire building blocks," *Science*, vol. 294, no. 5545, pp. 1313-1317, Nov 2001.

- [12] D. A. Wharam *et al.*, "ONE-DIMENSIONAL TRANSPORT AND THE QUANTIZATION OF THE BALLISTIC RESISTANCE," *Journal of Physics C-Solid State Physics*, vol. 21, no. 8, pp. L209-L214, Mar 20 1988.
- [13] B. J. Vanwees *et al.*, "QUANTIZED CONDUCTANCE OF POINT CONTACTS IN A TWO-DIMENSIONAL ELECTRON-GAS," *Physical Review Letters*, vol. 60, no. 9, pp. 848-850, Feb 1988.
- [14] M. O. Manasreh and I. Wiley, *Introduction to Nanomaterials and Devices* (no. Book, Whole). Hoboken: Wiley-Interscience, 2012.
- [15] S. Datta, *Electronic transport in mesoscopic systems* (no. Book, Whole). Cambridge;New York;: Cambridge University Press, 1995.
- [16] A. S. Epstein, H. Fritzsche, and K. Larkhorovitz, "ELECTRICAL PROPERTIES OF TELLURIUM AT THE MELTING POINT AND IN THE LIQUID STATE," *Physical Review*, vol. 107, no. 2, pp. 412-419, 1957.
- [17] J. D. Joannopoulos, M. Schluter, and M. L. Cohen, "ELECTRONIC-STRUCTURE OF TRIGONAL AND AMORPHOUS SE AND TE," *Physical Review B*, vol. 11, no. 6, pp. 2186-2199, 1975 1975.
- [18] R. M. Martin, G. Lucovsky, and K. Helliwell, "INTERMOLECULAR BONDING AND LATTICE-DYNAMICS OF SE AND TE," *Physical Review B*, vol. 13, no. 4, pp. 1383-1395, 1976.
- [19] B. Z. Wu, X. H. Liu, J. R. Yin, and H. Lee, "Bulk beta-Te to few layered beta-tellurenes: indirect to direct band-Gap transitions showing semiconducting property," *Materials Research Express*, vol. 4, no. 9, Sep 2017, Art.no. 095902.
- [20] E. Andharia, T. P. Kaloni, G. J. Salamo, S. Q. Yu, O. H. Churchill, and S. Barraza-Lopez, "Exfoliation energy, quasiparticle band structure, and excitonic properties of selenium and tellurium atomic chains," *Physical Review B*, vol. 98, no. 3, Jul 2018, Art. no. 035420.
- [21] X. C. Huang *et al.*, "Epitaxial Growth and Band Structure of Te Film on Graphene," *Nano Letters*, vol. 17, no. 8, pp. 4619-4623, Aug 2017.
- [22] T. Tani and S. Tanaka, "Pressure effect on the impurity state and impurity conduction in tellurium," *Physics of Selenium and Tellurium*, pp. 142-52, 1979 1979.

- [23] Y. C. Du *et al.*, "One-Dimensional van der Waals Material Tellurium: Raman Spectroscopy under Strain and Magneto-Transport," *Nano Letters*, vol. 17, no. 6, pp. 3965-3973, Jun 2017.
- [24] S. Nadj-Perge, S. M. Frolov, E. Bakkers, and L. P. Kouwenhoven, "Spin-orbit qubit in a semiconductor nanowire," *Nature*, vol. 468, no. 7327, pp. 1084-1087, Dec 2010.
- [25] "Proceedings of the International Symposium on the physics of selenium and tellurium," *Proceedings of the International Symposium on the physics of selenium and tellurium*, pp. ix+380 pp-ix+380 pp, 1969 1969.
- [26] Y. X. Wang *et al.*, "Field-effect transistors made from solution-grown two-dimensional tellurene," *Nature Electronics*, vol. 1, no. 4, pp. 228-236, Apr 2018.
- [27] H. S. Qian, S. H. Yu, J. Y. Gong, L. B. Luo, and L. F. Fei, "High-quality luminescent tellurium nanowires of several nanometers in diameter and high aspect ratio synthesized by a poly (vinyl pyrrolidone)-assisted hydrothermal process," *Langmuir*, vol. 22, no. 8, pp. 3830-3835, Apr 11 2006.
- [28] G. C. Xi, Y. K. Liu, X. Q. Wang, X. Y. Liu, Y. Y. Peng, and Y. T. Qian, "Large-scale synthesis, growth mechanism, and photoluminescence of ultrathin Te nanowires," *Crystal Growth & Design*, vol. 6, no. 11, pp. 2567-2570, Nov 2006.
- [29] Y. J. Zhu, W. W. Wang, R. J. Qi, and X. L. Hu, "Microwave-assisted synthesis of single-crystalline tellurium nanorods and nanowires in ionic liquids," *Angewandte Chemie-International Edition*, vol. 43, no. 11, pp. 1410-1414, 2004.
- [30] L. Yang, Z. G. Chen, G. Han, L. N. Cheng, H. Y. Xu, and J. Zou, "Trifold Tellurium One-Dimensional Nanostructures and Their Formation Mechanism," *Crystal Growth & Design*, vol. 13, no. 11, pp. 4796-4802, Nov 2013.
- [31] S. Sen *et al.*, "Synthesis of tellurium nanostructures by physical vapor deposition and their growth mechanism," *Crystal Growth & Design*, vol. 8, no. 1, pp. 238-242, Jan 2008.
- [32] C. J. Hawley, B. R. Beatty, G. N. Chen, and J. E. Spanier, "Shape-Controlled Vapor-Transport Growth of Tellurium Nanowires," *Crystal Growth & Design*, vol. 12, no. 6, pp. 2789-2793, Jun 2012.

- [33] V. V. Poborchii, "Polarized Raman and optical absorption spectra of the mordenite single crystals containing sulfur, selenium, or tellurium in the one-dimensional nanochannels," *Chemical Physics Letters*, vol. 251, no. 3-4, pp. 230-234, Mar 22 1996.
- [34] V. V. Poborchii, M. S. Ivanova, V. P. Petranovskii, Y. A. Barnakov, A. Kasuya, and Y. Nishina, "Raman and absorption spectra of the zeolites A and X containing selenium and tellurium in the nanopores," *Materials Science and Engineering a-Structural Materials Properties Microstructure and Processing*, vol. 217, pp. 129-134, Oct 30 1996.
- [35] K. Kobayashi and H. Yasuda, "Structural transition of tellurium encapsulated in confined one-dimensional nanospaces depending on the diameter," *Chemical Physics Letters*, vol. 634, pp. 60-65, Aug 2015.
- [36] P. V. C. Medeiros *et al.*, "Single-Atom Scale Structural Selectivity in Te Nanowires Encapsulated Inside Ultranarrow, Single-Walled Carbon Nanotubes," *Acs Nano*, vol. 11, no. 6, pp. 6178-6185, Jun 2017.
- [37] Y. Yu *et al.*, "Room temperature rubbing for few-layer two-dimensional thin flakes directly on flexible polymer substrates," *Scientific Reports*, vol. 3, Sep 18 2013, Art. no. 2697.
- [38] A. S. Pine and G. Dresselhaus, "RAMAN SPECTRA AND LATTICE DYNAMICS OF TELLURIUM," *Physical Review B-Solid State*, vol. 4, no. 2, pp. 356+, 1971.
- [39] R. S. Caldwell and H. Y. Fan, "OPTICAL PROPERTIES OF TELLURIUM AND SELENIUM," *Physical Review*, vol. 114, no. 3, pp. 664-675, 1959.
- [40] P. T. Araujo, C. Fantini, M. M. Lucchese, M. S. Dresselhaus, and A. Jorio, "The effect of environment on the radial breathing mode of supergrowth single wall carbon nanotubes," *Applied Physics Letters*, vol. 95, no. 26, Dec 2009, Art. no. 261902.
- [41] W. Richter, J. B. Renucci, and M. Cardona, "HYDROSTATIC PRESSURE-DEPENDENCE OF FIRST-ORDER RAMAN FREQUENCIES IN SE AND TE," *Physica Status Solidi B-Basic Research*, vol. 56, no. 1, pp. 223-229, 1973.
- [42] J. Stuke and H. Keller, "Optical properties and band structure in the system Se-Te," *Phys Status Solidi*, vol. 7, p. 189, 1964.

- [43] R. Fubo, L. Wen, and D. Lixin, "Layer engineering of graphene with oxygen plasma etching," *2011 IEEE 11th International Conference on Nanotechnology (IEEE-NANO)*, pp. 1201-4, 2011 2011.
- [44] J. L. Xiao *et al.*, "Alignment Controlled Growth of Single-Walled Carbon Nanotubes on Quartz Substrates," *Nano Letters*, vol. 9, no. 12, pp. 4311-4319, Dec 2009.
- [45] H. Xu *et al.*, "Oscillating edge states in one-dimensional MoS₂ nanowires," *Nature Communications*, vol. 7, Oct 2016, Art. no. 12904.
- [46] O. Kiowski, S.-S. Jester, S. Lebedkin, Z. Jin, Y. Li, and M. M. Kappes, "Photoluminescence spectral imaging of ultralong single-walled carbon nanotubes: Micromanipulation-induced strain, rupture, and determination of handedness," *Physical Review B*, vol. 80, no. 7, Aug 2009, Art. no. 075426.
- [47] J. Lefebvre, D. G. Austing, J. Bond, and P. Finnie, "Photoluminescence imaging of suspended single-walled carbon nanotubes," *Nano Letters*, vol. 6, no. 8, pp. 1603-1608, Aug 9 2006.
- [48] J. Qin *et al.*, "Controlled Growth of a Large-Size 2D Selenium Nanosheet and Its Electronic and optoelectronic Applications," *Acs Nano*, vol. 11, no. 10, pp. 10222-10229, Oct 2017.
- [49] Q. Wang, G.-D. Li, Y.-L. Liu, S. Xu, K.-J. Wang, and J.-S. Chen, "Fabrication and growth mechanism of selenium and tellurium nanobelts through a vacuum vapor deposition route," *Journal of Physical Chemistry C*, vol. 111, no. 35, pp. 12926-12932, Sep 6 2007.
- [50] K. Nagata, K. Ishibashi, and Y. Miyamoto, "RAMAN AND INFRARED-SPECTRA OF RHOMBOHEDRAL SELENIUM," *Japanese Journal of Applied Physics*, vol. 20, no. 3, pp. 463-469, 1981.
- [51] Z. M. Liao, C. Hou, L. P. Liu, and D. P. Yu, "Temperature Dependence of Photoelectrical Properties of Single Selenium Nanowires," *Nanoscale Research Letters*, vol. 5, no. 6, pp. 926-929, Jun 2010.
- [52] M. Lucht *et al.*, "Precise measurement of the lattice parameters of alpha-Al₂O₃ in the temperature range 4.5-250 K using the Mossbauer wavelength standard," *Journal of Applied Crystallography*, vol. 36, pp. 1075-1081, Aug 2003.

- [53] G. Y. Zhou *et al.*, "High-Mobility Helical Tellurium Field-Effect Transistors Enabled by Transfer-Free, Low-Temperature Direct Growth," *Advanced Materials*, vol. 30, no. 36, Sep 2018, Art. no. 1803109.
- [54] Q. S. Wang, M. Safdar, K. Xu, M. Mirza, Z. X. Wang, and J. He, "Van der Waals Epitaxy and Photoresponse of Hexagonal Tellurium Nanoplates on Flexible Mica Sheets," *Acs Nano*, vol. 8, no. 7, pp. 7497-7505, Jul 2014.
- [55] M. Amani *et al.*, "Solution-Synthesized High-Mobility Tellurium Nanoflakes for Short-Wave Infrared Photodetectors," *Acs Nano*, vol. 12, no. 7, pp. 7253-7263, Jul 2018.
- [56] G. Qiu *et al.*, "Quantum Transport and Band Structure Evolution under High Magnetic Field in Few-Layer Tellurene," *Nano Letters*, vol. 18, no. 9, pp. 5760-5767, Sep 2018.
- [57] A. Daire, "An Improved Method for Differential Conductance Measurements " Keithley Instruments, Inc.2005.
- [58] E. J. Zimney, G. H. B. Dommett, R. S. Ruoff, and D. A. Dikin, "Correction factors for 4-probe electrical measurements with finite size electrodes and material anisotropy: a finite element study," *Measurement Science and Technology*, vol. 18, no. 7, pp. 2067-2073, Jul 2007.
- [59] H. L. Stormer, A. C. Gossard, and W. Wiegmann, "OBSERVATION OF INTERSUBBAND SCATTERING IN A TWO-DIMENSIONAL ELECTRON-SYSTEM," *Solid State Communications*, vol. 41, no. 10, pp. 707-709, 1982 1982.
- [60] J. Kammhuber *et al.*, "Conductance Quantization at Zero Magnetic Field in InSb Nanowires," *Nano Letters*, vol. 16, no. 6, pp. 3482-3486, Jun 2016.
- [61] F. C. Lu *et al.*, "Magneto-transport Spectroscopy of the First and Second Two-dimensional Subbands in Al_{0.25}Ga_{0.75}N/GaN Quantum Point Contacts," *Scientific Reports*, vol. 7, Feb 2017, Art. no. 42974.
- [62] V. B. Ansin *et al.*, "Influence of hydrostatic pressure on the splitting of the Landau levels in tellurium," *Sov. Phys. JETP*, vol. 38, no. 4, pp. 755-758, 1973.
- [63] F. Qu *et al.*, "Quantized Conductance and Large g-Factor Anisotropy in InSb Quantum Point Contacts," *Nano Letters*, vol. 16, no. 12, pp. 7509-7513, Dec 2016.

[64] K. Sattler, *Carbon Nanomaterials Sourcebook: Graphene, Fullerenes, Nanotubes, and Nanodiamonds, Volume I*. CRC Press, 2016.

[65] S. A. Dayeh, D. P. R. Aplin, X. T. Zhou, P. K. L. Yu, E. T. Yu, and D. L. Wang, "High electron mobility InAs nanowire field-effect transistors," *Small*, vol. 3, no. 2, pp. 326-332, Feb 2007.

[66] J. L. Chen, Y. W. Dai, Y. Q. Ma, X. Q. Dai, W. K. Ho, and M. H. Xie, "Ultrathin beta-tellurium layers grown on highly oriented pyrolytic graphite by molecular-beam epitaxy," *Nanoscale*, vol. 9, no. 41, pp. 15945-15948, Nov 2017.

Appendix

Gold markers and metal contacts were fabricated by the following recipe (Table A). The resists were baked before and after each resist coating.

Table A: Gold makers and metal contacts recipe

Device		1-JA and 1-WI	2-SF
Resist coating	Resist	1st: MMA 2nd: PMM	1st: MMA 2nd: CSAR/Anisole(1:1)
	Coating speed [rpm]	4000	4000
	Coating time [min]	1	1
Resist baking	Temperature [°C]	100	140
	Time [min]	10	5
	Environment	Atmosphere	Inside glovebox
Gold markers	Develop	MIBK/IPA 20min	n-amyl acetete 30s MIBK/IPA 45s
	Metal deposit	Cr 1nm	Cr 0.9nm
		Au 50nm	Au 60nm
Lift off	Acetone	Remover1165/Acetone (1:1)	
Contacts	Develop	MIBK/IPA 60s	n-amyl acetete 30s MIBK/IPA 45s
	Metal deposit	Cr 0.9 nm (30deg angled)	Cr 0.9 nm
		Au 100 nm (30deg angled)	Au 120 nm
Lift-off	Solution	Acetone	Remover1165/Acetone (1:1)